



POLITECNICO
MILANO 1863

Space System Engineering And Operations
Prof. Lavagna

Team n°4

SOHO Mission



Surname	Name	Mat.	Pers. Code
Pacursa	Andrea Jimmy	243771	10717720
Paltani	Davide	258731	10715533
Persenico	Francesco	247170	10733354
Piraccini	Mattia	244717	10765924
Portantiolo	Matteo	250184	10766648
Provenzi	Davide	247834	10731827

Contents

Nomenclature	IV
List of Figures	X
List of Tables	XI
1 Mission Overview and Mission Analysis	1
1.1 Introduction	1
1.2 High level goals	1
1.3 Mission Drivers	1
1.4 Payloads	2
1.5 Functional analysis	4
1.6 Main phases and ConOps	4
1.6.1 Main phases	4
1.6.2 ConOps	5
1.7 Mission analysis	5
2 Mission Trajectory Design and Propulsion Subsystem	7
2.1 Mission Trajectory Design	7
2.1.1 Launch and LEOP	7
2.1.2 Mid-course corrections	7
2.1.3 Halo Orbit Insertion and Station Keeping	7
2.1.4 Overall mission budget evaluation	7
2.1.5 Comparison with similar missions	8
2.2 Propulsion Architecture	9
2.3 Reverse Sizing	11
2.3.1 Propellant and pressurizer selection	11
2.3.2 Mass Breakdown	11
2.4 Comparison with the real system	13
3 Tracking, Telemetry and Telecommunication Subsystem	14
3.1 Architecture	14
3.1.1 Configuration rationale	14
3.2 Time windows and phases	15
3.3 Encoding and Modulation	15
3.4 SNR and Link Budget	16
3.4.1 Gain and losses calculation	17
3.5 Transmitted and input power and amplifier selection	17
3.6 Uplink communications during Safe Mode	18
3.7 Data volume	18
3.8 Channel capacity verification	19
3.9 Results	19
3.10 Conclusions and comparison	19
4 Attitude and Orbit Control Subsystem	21
4.1 Architecture	21
4.2 Design rationale	22
4.3 Control Modes	23
4.3.1 Normal Mode (NM)	23
4.3.2 ESR Mode (Emergency Sun Reacquisition)	23
4.3.3 CRP Mode (Coarse Roll Pointing)	24
4.3.4 RMW Mode (Roll Maneuver Wheels)	24

4.4	Sizing	24
4.4.1	Inertial properties	25
4.4.2	Disturbances	25
4.4.3	SRP compensation	26
4.4.4	Slew manoeuvre	27
4.5	Conclusions	27
5	Thermal Control Subsystem	28
5.1	Introduction	28
5.2	Basic Configuration	28
5.3	Architecture	28
5.4	Single-Node Analysis	29
5.4.1	Assumptions and properties	29
5.4.2	Hot and cold case selection	30
5.4.3	Hot Case	30
5.4.4	Cold Case	31
5.5	Multi-Nodal Analysis	31
5.5.1	Model definition	31
5.5.2	Sizing	32
5.6	System Budgets	33
5.6.1	Mass Budget	33
5.6.2	Data Budget	33
5.6.3	Power Budget	33
6	Electric Power Subsystem	34
6.1	Introduction	34
6.2	Architecture	34
6.2.1	Architecture rationale	34
6.3	Sizing	34
6.3.1	Solar Array	35
6.3.2	Batteries	38
6.4	Budgets	39
6.4.1	Data Budget	39
6.4.2	Mass and Volume Budget	39
7	Configuration	40
7.1	General considerations	40
7.1.1	Folded configuration	40
7.2	Payload Module	40
7.2.1	Scientific instruments	40
7.2.2	PLM Sensors and Electronics	41
7.3	Service Module	41
7.3.1	Propulsion subsystem	42
7.3.2	Service Equipment Module	42
8	On-Board Data Handling Subsystem	43
8.1	Architecture	43
8.2	Sizing	44
8.2.1	Throughput Sizing	44
8.2.2	Memory Sizing	46
References		ii
Appendix		iii
Appendix A - Chapter 4		iii
Appendix B - Chapter 5		iv

Appendix C - Chapter 7	v
Appendix D - Chapter 8	vi

Nomenclature

A

\mathbf{a}_{SRP} Acceleration due to solar radiation pressure $[\frac{m}{s^2}]$

α Absorptivity [-]

A_{sun} S/C's surface facing the Sun $[m^2]$

B

B Bandwidth $[MHz]$

B Blowdown ratio [-]

C

C Capacity $[Wh]$

c Speed of light $[\frac{m}{s}]$

c_g Center of gravity $[m]$

c_p Center of pressure $[m]$

c_r Reflectivity coefficient [-]

D

Δv Manoeuvre cost $[\frac{m}{s}]$

dpy Degradation per year [-]

E

ϵ_{BOL} Efficiency of solar array cells [-]

ϵ_{rad} Emissivity [-]

η Efficiency [-]

E_m Specific Energy $\left[\frac{Wh}{Kg}\right]$

E_v Energy density $[\frac{Wh}{dm^3}]$

F

f Frequency $[Hz]$

$F_{1 \rightarrow 2}$ View factor from surface 1 to surface 2 $[\frac{m}{s}]$

G

G Gain $[dB]$

g_0 Gravitational acceleration on Earth $[\frac{m}{s^2}]$

H

h angular momentum [Nms]

I

\mathbf{I} Inertia matrix

I_d inherent degradation factor [−]

I_{sp} Specific impulse [s]

L

L Losses [dBW]

M

μ Package efficiency [−]

M Torque [Nm]

m Mass [kg]

M_{SRP} Momentum disturbance from Solar radiation pressure [Nm]

N

N Noise [W]

P

p Specific power [$\frac{W}{m^2}$]

P_{rx} Received power [W]

$p_{SRP,1AU}$ Incoming radiation pressure from the Sun at a 1 AU distance [$\frac{N}{m^2}$]

P_{tx} Transmitted power [W]

P Power [W]

Q

\dot{Q} Heat flux [W]

\dot{q} Heat flux per unit area [W/m^2]

q Reflectivity coefficient [−]

R

\mathbf{r}_{SC-Sun} Relative position vector of the SC with respect to the Sun [km]

R Thruster configuration matrix [m]

ρ Density $\left[\frac{kg}{m^3}\right]$

R Universal gas constant $\left[\frac{J}{kgK}\right]$

S

σ Ultimate tensile strength [MPa]
 σ_0 Stefan-Boltzmann constant [$\frac{W}{m^2 K^4}$]

T

T Thrust [N]
 t Thickness [mm]

U

U Voltage [V]

V

V Volume [m^3]
 v Speed [$\frac{m}{s}$]

X

X_d Line efficiency [-]

Acronyms

ACU Attitude Control Unit
ANTS ANTenna Subsystem
AOS Acquisition Of Signal
APE Absolute Performance Error
BER Bit Error Rate
BOL Beginning Of life
BSR Back Surface Reflection
CDMU Central Data Memory Unit
CDS Coronal Diagnostic Spectrometer
CELIAS Charge Element and Isotope Analysis System
COBS Central On-Board Software
CoM Center of Mass
COSTEP Comprehensive Suprathermal and Energetic Particle Analyzer
DET Direct Energy Transfer
DHSS Data Handling SubSystem
DOD Depth of Discharge
DSM Deep Space Manoeuvre

DSN Deep Space Network
EAF Experiment Analysis Facilities
ECI Earth Centred Inertial reference frame
ECSS European Cooperation for Space Standardization
EIT Extreme ultraviolet Imaging Telescope
EOF Experiment Operations Facility
EOL End Of Life
EOM Equation Of Motion
EPS Electrical Power Subsystem
ERNE Energetic and Relativistic Nuclei and Electron experiment
ESR Emergency Sun Reacquisition
EUV Extreme Ultraviolet
FOV Field Of View
FPSS Fine Pointing Sun Sensor
FSS Fine Sun Sensor
GOLF Global Oscillations at Low Frequencies
GS Ground Station
HGA High Gain Antenna
HOI Halo Orbit Injection
HOP Halo Orbit Phase
IPS Instructions Per Second
IR Infrared Radiation
IRU Inertial Reference Unit
ISA Initial Sun Acquisition
L1 First Lagrangian Point
LASCO Large Angle and Spectrometric COronagraph
LEOP Launch and Early Orbit Phase
LGA Low Gain Antenna
LPO Libration Point Orbit
MACS Modular Attitude Control Systems

MCC Mid-Course Correction

MDI Michelson Doppler Imager

MECO Main Engine Cut-Off

MES Main Engine Start

MMM Momentum Management Maneuver

MR Mass ratio

OBDHS On-Board Data Handling

OBT On-Board Time

OSR Optical Solar Reflector

P/L Payload

PDU Power Distribution Unit

PEP Peripheral Expansion Port

PLM Payload Module

PPT Peak Power Transfer

PROM Programmable Read Only Memory

RAM Random Access Memory

RLP Rotating Libration Point

ROM Read Only Memory

RTU Remote Terminal Unit

RW Reaction Wheel(s)

S/C Spacecraft

S/S Subsystem

SA Solar Array

SAS Solar Acquisition Sensor

SEE Single Event Effect

SEV Sun – Earth – Vehicle

SEZ Solar Exclusion Zone

SGS Solar Generator Subsystem

SHS Structure and Harness Subsystem

SK Station Keeping

SNR Signal to Noise Ratio

SPAAD Sun Pointing Attitude Anomaly Detector

SSA Solid State Amplifier

SSU Star Sensor Unit

SUMER Solar Ultraviolet Measurement of Emitted Radiation

SVM Service Module

SWAN Solar Wind Anisotropies

TCM Trajectory Control Manoeuvre

TP Throughput

TTI Transfer Trajectory Insertion

TTP Transfer Trajectory Phase

UVCS UltraViolet Coronagraph Spectrometer

VIRGO Variability of Solar IRradiance and Gravity Oscillations

List of Figures

1	SOHO spacecraft schematic view	3
2	Functional Analysis	4
3	Main phases and ConOps (not to scale)	5
4	Transfer orbit overview	5
5	Side View of Libration Point Orbits with Solar Exclusion Zone visualization	6
6	SOHO mission overview; from launch to orbit insertion	6
7	Propulsion subsystem architecture	9
8	Pressure-fed vs Turbopump-fed	10
9	Antennae configuration	14
10	Amplifier efficiency	18
11	Payloads disposition	25
12	Electrical Scheme	32
13	SA actual configuration	37
14	EPS Telemetry parameters	39
15	General configuration	40
16	PLM sensors and scientific instruments disposition	41
17	Propulsion module	42
18	SVM layout	42
19	OBDH Scheme	43
20	CDMU and OBDH overview	43
21	Memory partition	44
22	Total throughput needed by each S/S without AOCS	45
23	Total throughput needed by AOCS	45
24	Evolution of processors for space applications	45
25	S/C dimensions and thrusters configuration	iii
26	Payload Module without sun shield	v
27	Tilted configuration	v
28	Acquisition frequency and KIPS of all subsystems without AOCS	vi
29	Acquisition frequency and KIPS of AOCS	vi

List of Tables

1	High Level Goals	1
2	Goals - P/Ls	3
3	Δv breakdown from estimation	8
4	Comparison between missions	8
5	Thruster data	10
6	Thrusters position and direction	10
7	Materials properties	12
8	Mass breakdown	13
9	Data comparison with real system	13
10	Downlink and Uplink numerical results	19
11	Comparison with real data for downlink configuration	20
12	Comparison with real data for uplink configuration	20
13	On-board sensors and actuators	21
14	Pointing and Alignment Parameters	22
15	RW data	24
16	Payloads weights	25
17	Solar pressure data	26
18	Constants and thermo-optical properties	29
19	View factors	32
20	Nodes' temperatures	32
21	Power Budget	35
22	SA sizing data	35
23	Solar Cells data	36
24	SA layers data	36
25	Single Battery data	38
26	PROM and RAM size for OBDH and AOCS	46
27	Thrusters position and direction	iii

1 Mission Overview and Mission Analysis

1.1 Introduction

SOHO, the Solar and Heliospheric Observatory, is a project of international cooperation between ESA and NASA to study the Sun, from its deep core to the outer corona, and the solar wind.

Launched in December 1995, originally planned as a two-year mission, SOHO continues to operate after over 25 years in space; the mission has been extended until the end of 2025.

Together with two other ESA missions, Cluster and Ulysses, SOHO is studying the Sun-Earth interaction from different perspectives. It constantly watches the Sun, returning pictures and data of the storms that rage across its surface. SOHO's studies range from the Sun's hot interior, through its visible surface and stormy atmosphere, and out to distant regions where the wind from the Sun battles with a breeze of atoms coming from among the stars.

SOHO is often described as the biggest discoverer of comets, with more than 4000 bodies discovered.

1.2 High level goals

Guiding question	Science objectives
What is the structure and what are the dynamics of the solar interior?	Study of the structure and dynamics of the solar interior through the observation of minute oscillations on the sun's surface (helioseismology).
Why does the corona (the tenuous outer solar atmosphere that can be seen with naked eye during eclipses and which is much hotter than the solar surface) exist and how it is heated?	Solar spectroscopy at soft X-ray and EUV wavelengths (study of the composition of the solar corona, of the structure and dynamics of the magnetic structures making up the corona, of coronal holes, etc.)
Where and how is the solar wind, i.e. the particle streams which represent the solar mass loss, accelerated?	Study of the solar wind and solar energetic particles, interaction with the Earth, plasma processes in both the solar and magnetospheric context.

Table 1: High Level Goals

1.3 Mission Drivers

The drivers of a mission are critical requirements that lead completely or partly the design process of one or more subsystems. For the SOHO mission, the following drivers have been recognized:

- **Sun pointing:** The S/C shall be able to keep a steady pointing along the Sun direction and guarantee high accuracy, to satisfy the high-level goals of the mission. In order to do that, two Fine Sun Sensors (FSS) are used.
- **Communications:** The satellite shall be able to communicate in real-time with the Deep Space Network (DSN) ground stations. SOHO has one High-Gain Antenna (HGA) to allow the download of high-rate data and two low-gain antennae mounted on fixed booms at the bottom section of the service module that protrude from the main body to provide full geometrical coverage.

- **Environment:** In order to have both a steady and accurate pointing along the Sun direction and real-time communication with the GS the S/C's orbit will be around L1, which provides a perfect vantage point for the required investigation. The satellite is located outside the absorbing, blurring and scattering terrestrial atmosphere and outside the magnetic shield of the Earth's magnetosphere. Consequently, SOHO is subjected to the entire electromagnetic and particle spectrum of the Sun but this implies the presence of the solar wind on the satellite, which shall be taken into account during the design of the whole system.

1.4 Payloads

The spacecraft carried 12 payloads for scientific purposes:

- **Coronal Diagnostic Spectrometer (CDS):** detects emission lines from ions and atoms in the solar corona and transition region, providing diagnostic information on the solar atmosphere, especially of the plasma in the temperature range from 10 000 to more than 1 000 000°C.
- **Charge Element and Isotope Analysis System (CELIAS):** CELIAS continuously samples the solar wind and energetic ions of solar, interplanetary and interstellar origin, as they sweep past SOHO. It analyses the density and composition of particles present in this solar wind. It warns of incoming solar storms that could damage satellites in Earth orbit.
- **Solar Ultraviolet Measurement of Emitted Radiation (SUMER):** used to perform detailed spectroscopic plasma diagnostics (flows, temperature, density, and dynamics) of the solar atmosphere, from the chromosphere through the transition region to the inner corona, over a temperature range from 10 000 to 2 000 000°C and above.
- **Michelson Doppler Imager (MDI):** records the vertical motion (“tides”) of the Sun’s surface at a million different points for each minute. By measuring the acoustic waves inside the Sun as they perturb the photosphere, scientists can study the structure and dynamics of the Sun’s interior. The MDI also measures the longitudinal component of the Sun’s magnetic field.
- **Global Oscillations at Low Frequencies (GOLF):** studies the internal structure of the Sun by measuring velocity oscillations over the entire solar disc.
- **Comprehensive Suprathermal and Energetic Particle Analyzer (COSTEP):** detects and classifies very energetic particle populations of solar, interplanetary, and galactic origin. It is a complementary instrument to ERNE.
- **Energetic and Relativistic Nuclei and Electron experiment (ERNE):** measures high-energy particles originating from the Sun and the Milky Way.
- **Extreme ultraviolet Imaging Telescope (EIT):** provides full disc images of the Sun at four selected colours in the extreme ultraviolet, mapping the plasma in the low corona and transition region at temperatures between 80 000 and 2 500 000°C.
- **UltraViolet Coronagraph Spectrometer (UVCS):** makes measurements in ultraviolet light of the solar corona (between about 1.3 and 12 solar radii from the centre) by creating an artificial solar eclipse. It blocks the bright light from the solar disc and allows observation of the less intense emission from the extended corona. UVCS provides valuable information about the microscopic and macroscopic behaviour of the highly ionised coronal plasma.
- **Large Angle and Spectrometric Coronagraph (LASCO):** observes the outer solar atmosphere (corona) from near the solar limb to a distance of 21 million kilometres, that is, about one seventh of the distance between the Sun and the Earth. LASCO blocks direct light from the surface of the Sun with an occulter, creating an artificial eclipse, 24 hours a day, 7 days a week. LASCO has also become SOHO’s principal comet finder.
- **Variability of solar IRradiance and Gravity Oscillations (VIRGO):** characterises solar intensity oscillations and measures the total solar irradiance to quantify its variability over periods of days to the duration of the mission.

- **Solar Wind Anisotropies (SWAN)**: is the only remote sensing instrument on SOHO that does not look at the Sun. It watches the rest of the sky, measuring hydrogen that is "blowing" into the Solar System from interstellar space. By studying the interaction between the solar wind and this hydrogen gas, SWAN determines how the solar wind is distributed. As such, it can be qualified as SOHO's solar wind "mapper".

Goals	Payloads
Helioseismology	Two velocity spectrometers (GOLF and MDI) and several radiometers (VIRGO), that can measure the velocity and intensity of solar oscillations, investigate non-periodic variations of the solar "constant", and determine its absolute value.
Coronagraphy	A number of remote-sensing instruments (CDS, EIT, LASCO, SUMER, UVCS) are designed to study the physical structure and dynamics of the upper solar atmosphere (i.e. the so-called 'chromosphere', 'transition zone' and 'corona', out to 30 solar radii); it also surveys (out to at least 10 AU) the ionised cavity which the solar wind "burns" into the neutral "stellar wind" that traverses the heliosphere (SWAN).
Solar-wind and particles analysis	Several mass-spectrometers (CELIAS) and medium- and high-energy particle analysers (COSTEP, ERNE) are used to study the solar wind in-situ, near the Earth's orbit (more precisely at 0.99 AU), and to investigate solar as well as cosmic energetic particles.

Table 2: Goals - P/Ls

The relationship between the investigations of the three questions listed initially and the three payload segments is not a strict one, because studies of the acceleration of the solar wind and of the structure of the corona require both remote and in-situ sensing of the solar-wind streams.

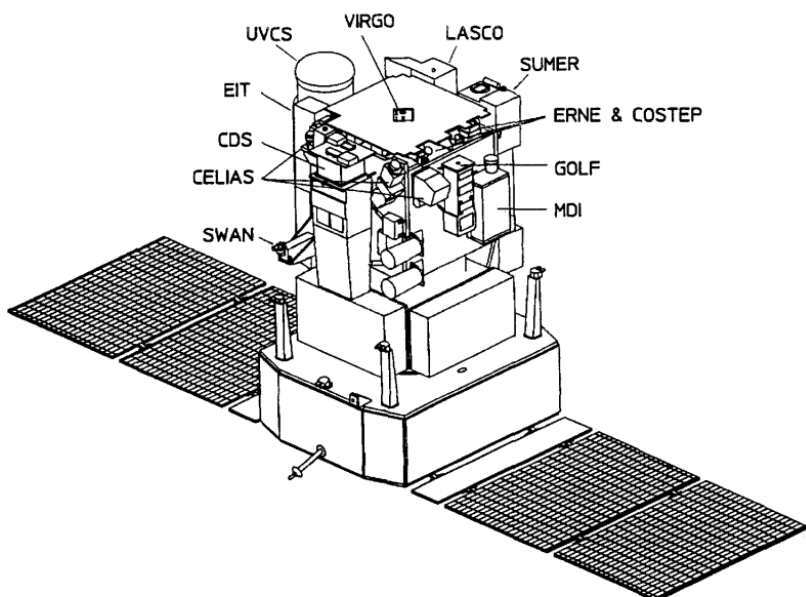


Figure 1: SOHO spacecraft schematic view

1.5 Functional analysis

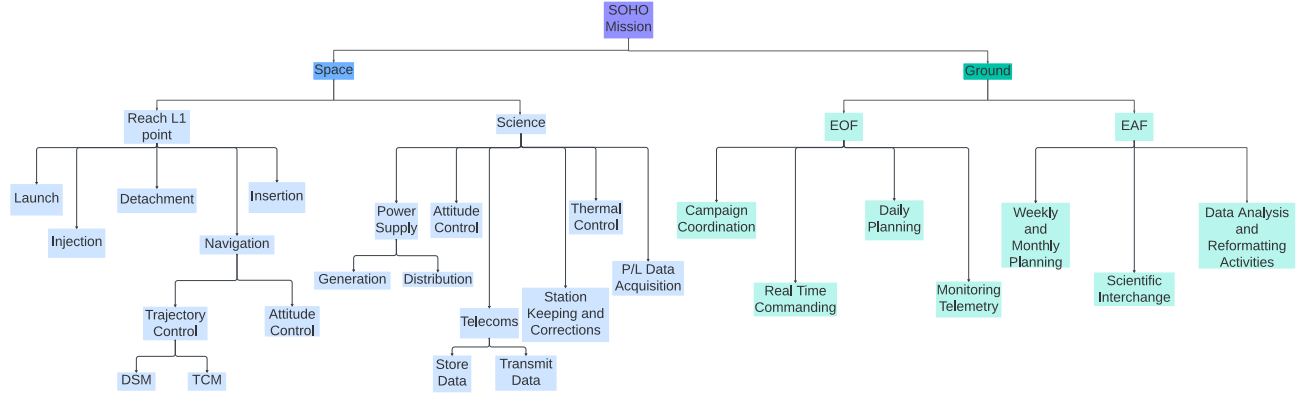


Figure 2: Functional Analysis

1.6 Main phases and ConOps

1.6.1 Main phases

The SOHO operational mission is mainly divided into three phases:

- Launch and Early Orbit Phase (LEOP)
- Transfer Trajectory Phase (TTP)
- Halo Orbit Phase (HOP)

Launch and Early Orbit Phase (LEOP) This phase starts at lift-off, includes the coasting period in parking orbit, and ends with the injection of the spacecraft into the transfer trajectory. During the LEOP phase, the SOHO/Centaur composite will be oriented with its X-axis towards the south ecliptic, with a roll rate of about 0.2 rpm. This attitude will be achieved and maintained by the Centaur upper stage. The latter will start the thermal roll soon enough after insertion into parking orbit and sufficiently late before transfer trajectory insertion for the spacecraft to be exposed to sunlight (from launcher payload fairing jettison until injection into transfer) for less than 8 min. No communication with the ground is foreseen during this phase.

Transfer Trajectory Phase (TTP) The TTP begins with the injection of the spacecraft into transfer orbit (MECO2) and ends with the injection into the halo orbit. It lasts about 4 months and, although science operations should be possible and will likely occur, priority will be given to the health and status of the spacecraft bus in this phase. The maximum duration for the first Acquisition of Signal (AOS) after injection into transfer trajectory is 35 min. Housekeeping and science telemetry, telecommand, and ranging links will be established during this phase.

Halo-Orbit Phase (HOP) The HOP starts at the spacecraft's injection into the halo orbit: after this insertion and the commissioning for all on-board instruments (part of this subphase may already have been performed during the TTP), a first station-keeping manoeuvre will be performed. Every 8 weeks, an orbit maintenance manoeuvre will be conducted. Momentum-wheel off-loading will be coupled with orbit correction manoeuvres. During this phase, the satellite will be three-axis-stabilised in a Sun-pointing attitude. In the case of safe-mode activation, it maintains this Sun-pointing attitude but to a lower accuracy.

1.6.2 ConOps

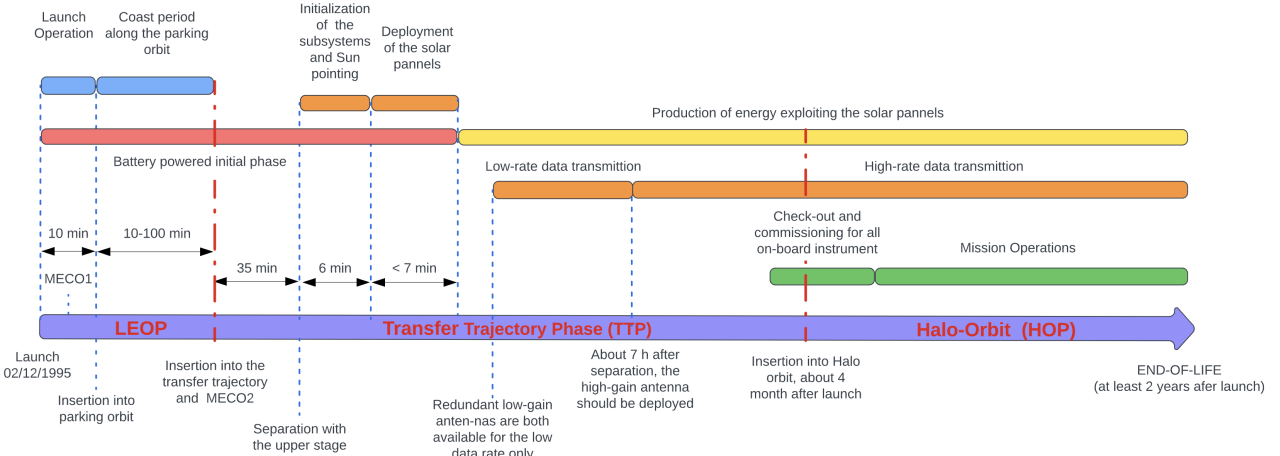


Figure 3: Main phases and ConOps (not to scale)

1.7 Mission analysis

The SOHO mission has been launched on the 2nd December 1995 on board of the Atlas II-AS launch system from Cape Canaveral Launch Complex 36.

The S/C followed a transfer trajectory for the first 4 months after launch, in order to reach the operating orbit. Figure 4 shows the transfer from two different points of view in space, together with the lunar orbit for comparison.

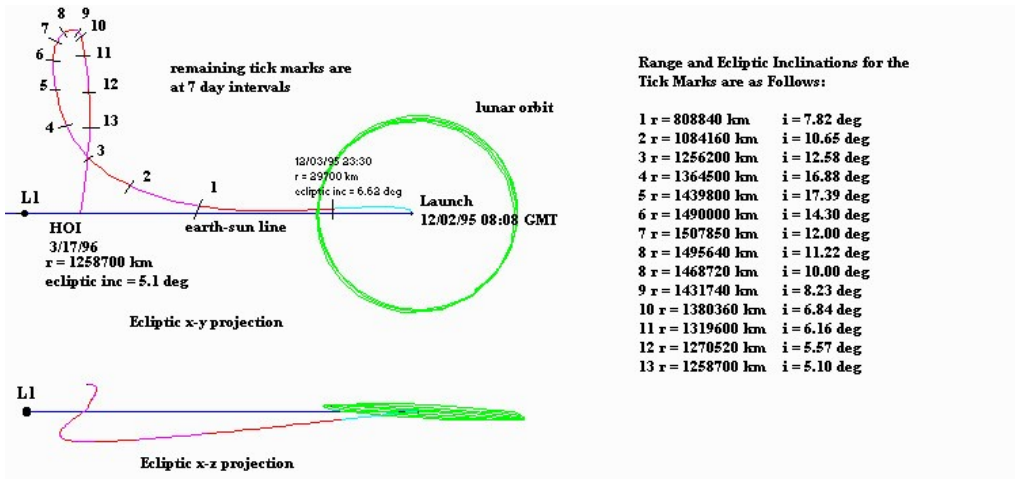


Figure 4: Transfer orbit overview

Being fundamental goals of the mission both Sun observation and continuous information flow directed to the Earth, a Libration Point Orbit (LPO) has been chosen as the operating orbit, located at the first libration point of the Earth-Sun system, L1. The Sun-Earth L1 point region is, in fact, the perfect location from which to conduct continuous, direct observation of the Sun and perform in-situ measurements of the upstream solar wind, while guaranteeing the continuity of telecommunications with ground.

The SOHO orbit is a quasi-periodic halo orbit, where the frequencies of the in-plane and out-of-plane motions are practically equal. Such an orbit is seen to repeat itself with a period of approximately 178 days.

The main constraint for the out-of-plane amplitude of such an orbit is the one associated with the Solar Exclusion Zone (SEZ). The SEZ is basically a right-circular cone of space with the Earth-Sun line for its axis, its vertex at Earth's center, and a specific angular radius at the distance of L1. This requirement exists so that the spacecraft can avoid solar radio frequency background interference with their downlink transmissions. To determine whether the spacecraft trajectories are in fact staying clear of their mission SEZ, the Sun-Earth-Vehicle (SEV) angle is monitored continuously throughout the mission. A SEZ violation would occur if the SEV angles over a portion of an orbit fall below the SEZ angle limit. The following figure shows a lateral view of how this constraint is satisfied.

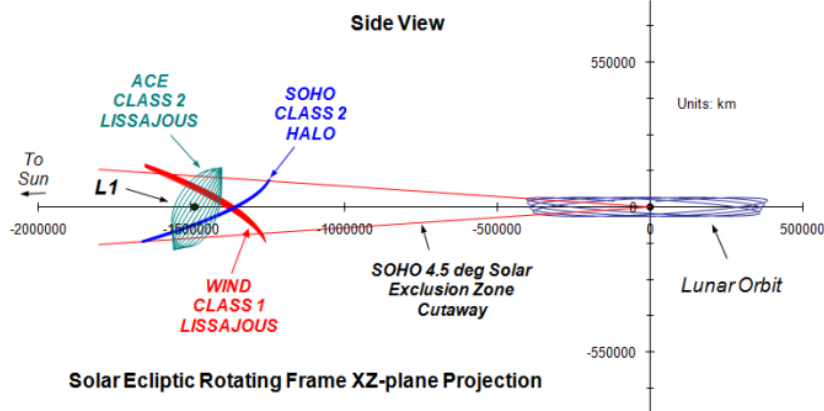


Figure 5: Side View of Libration Point Orbits with Solar Exclusion Zone visualization

The SOHO mission orbit is a Class 2-type halo orbit, the main characteristic of the Class 2 being that its sense of revolution about L1, as it appears from Earth, is counterclockwise. The primary mission constraints placed on the halo orbit were:

- that the minimum SEV angle never be less than 3° (the SEZ constraint)
- that the maximum SEV angle never be greater than 32° .

The maximum SEV constraint derives from the HGA gimbal angle limits and was also relevant in the design of the Earth to L1 transfer trajectory.

The halo orbit selected for SOHO during the pre-launch mission design phase satisfied the mission constraints with plenty of margin. The design results showed that for the six-year anticipated life of SOHO the orbit comes no closer to the solar center than 4.5° during the nearer, Earth-side crossing of the RLP XZ-plane¹, and is at about 5° at the farther, Sun-side crossing. At the RLP extreme Y-axis points of the halo, the SEV angle is never more than approximately 25.5° . The RLP-frame oscillation amplitudes corresponding to this 4.5 -by- 25.5 degree orbit, as specified during the pre-launch mission design phase, were as follows: $A_X = 206\,448 \text{ km}$, $A_Y = 666\,672 \text{ km}$, $A_Z = 120\,000 \text{ km}$.

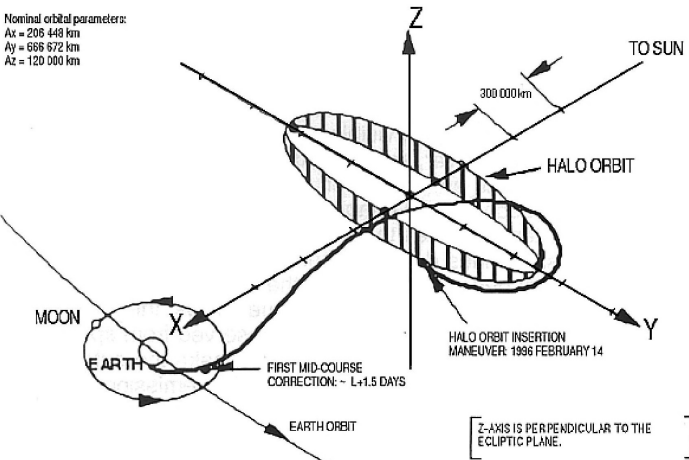


Figure 6: SOHO mission overview; from launch to orbit insertion

2 Mission Trajectory Design and Propulsion Subsystem

Change log	
§ 2.1.4	p.8 : Table 3 revised
§ 2.3.2	pp.11-13 : Added numerical results and initial data specification

2.1 Mission Trajectory Design

2.1.1 Launch and LEOP

The launch occurred on December 2nd at 08 : 08 : 00 GMT, a few minutes before the end of the window, due to hold during the countdown. The Atlas launch system ascended for approximately 10 minutes and delivered the Centaur/SOHO pair into a nearly-circular low-Earth parking orbit. Following a coasting phase of 74 minutes, the Centaur upper stage ignited (MES2) at the specified Transfer Trajectory Insertion (TTI) point and then shut down after 118 s (MECO2), placing the spacecraft on the transfer orbit. The actual separation of the Centaur upper stage happened 35 minutes after TTI due to DSN viewing requirements.

2.1.2 Mid-course corrections

During the transfer trajectory phase a few mid-course corrections were performed, in order to rectify the trajectory. Pre-mission analysis determined, in the worst case, MCC1 to be 30 m/s , but the actual manoeuvre was delayed and split into two manoeuvres of 3.04 m/s and 1.557 m/s , using thrusters 1 and 2. An additional mid-course correction was selected among 3 possible options. The final decision was to adopt a shaping manoeuvre instead of a simple error correction, in order to reduce the cost and the number of manoeuvres of the insertion into the final halo orbit (one x-segment of 6 m/s , using thrusters 1 and 2, and two z-segments of 15.7 m/s and 10.0 m/s , using thrusters 7 and 8)².

2.1.3 Halo Orbit Insertion and Station Keeping

In the beginning, a wide range of possible insertion dates were considered, in order to provide enough flexibility to counter possible errors and DSN scheduling. The HOI of 14 m/s was conducted on February 14th, paired with a trim manoeuvre in the order of 89 cm/s in the following weeks to fine tune the halo orbit.

Station keeping (SK) manoeuvres were set to be performed before the correction Δv grew to 0.5 m/s and were scheduled together with the momentum management manoeuvres (MMMs) [2][3].

Considering the first 8 SK manoeuvres, the average maintenance cost per year adds up to 2.49 m/s [3]. The following manoeuvres would require a dedicated analysis to understand the problem encountered with the safe mode activation and its relative recovery that are beyond the scope on this overview on the mission design.

2.1.4 Overall mission budget evaluation

In order to obtain a reliable value for the overall mission's Δv , the main manoeuvres have to be simulated along with their cost. Since the final aim is to size the propulsion subsystem for the SOHO S/C, only the manoeuvres performed after the MECO2 will be considered, which translates in taking into account only the contribution of the second impulsive manoeuvre in the approximated transfer computed.

For what regards the transfer trajectory, it is known from literature [4][5] that for such a transfer two MCCs are usually required, in order to reduce at the maximum the cost of the following HOI

²All manoeuvres' costs were taken from [1]

manoeuvre. However, in this case, a simple heliocentric Hohmann transfer has been selected as a rough first estimation, considering the starting point as the Earth's position and the arrival one as the opposite point on a circular orbit with radius equal to the distance between the Sun and L1.

Once entered in its operative halo orbit around L1, the S/C is subjected to the SRP, which has been considered as the main orbit perturbation. For this reason, frequent SK manoeuvres are required, and their magnitude can be estimated using the following model for the SRP perturbing acceleration:

$$\mathbf{a}_{\text{SRP}} = p_{\text{SRP},1AU} \left(\frac{AU}{\|\mathbf{r}_{\text{SC-Sun}}\|} \right)^2 c_R \frac{A_{\text{Sun}}}{m} \frac{\mathbf{r}_{\text{SC-Sun}}}{\|\mathbf{r}_{\text{SC-Sun}}\|} \quad (1)$$

Where $p_{\text{SRP},1AU} = 4.5 \cdot 10^{-6} \frac{N}{m^2}$ and c_R is set to be 1.2. Moreover, for simplicity's sake, the S/C is here assumed to be moving on a heliocentric circular orbit with the Sun-L1 distance as radius.

In order to avoid too frequent manoeuvres that could impact the accuracy of the measurements acquired by the P/L, a threshold of 0.5 m/s per manoeuvre has been taken into account for the SK manoeuvres. This constraint led to a schedule of the burns where each of them is set to happen approximately every 90 days once the S/C starts its nominal operations.

In addition to these two contributions, an additional 100 m/s one is considered to take into account eventual corrections to launch injection errors and for the HOI, and approximately 43 m/s are added as a budget for the attitude control manoeuvres [3] [6].

A breakdown of the total estimated Δv is reported in Table 3:

	$\Delta v_{MCC1}[\text{m/s}]$	$\Delta v_{MCC2}[\text{m/s}]$	$\Delta v_{HOI}[\text{m/s}]$	$\Delta v_{SK}[\text{m/s}]$	$\Delta v_{margin}[\text{m/s}]$	$\Delta v_{attitude}[\text{m/s}]$	$\Delta v_{tot}[\text{m/s}]$
Estimated	75			19.5	100	43	237.6

Table 3: Δv breakdown from estimation

It is important to underline that the obtained value differ from the official 318 m/s data [3]. This difference clearly means that this type of budget breakdown does not take into account all the margins and issues considered during the real mission design process. Such further considerations can be related to the fact that all L1 orbits are inherently unstable and some additional kind of periodical manoeuvres could be needed. Other missions, indeed, perform other kinds of manoeuvres, in order to counter the instability of the orbit, such as RLP z-axis manoeuvres (ACE - 20 \div 25 m/s/year [6]) and SEZ manoeuvres (DSCOVR - 25.6 m/s/year [7]).

2.1.5 Comparison with similar missions

In the following section a justification of the choices made for the Δv estimation is reported.

As previously mentioned, the Hohmann transfer is a rough approximation of the actual transfer to the halo orbit, including two MCCs and the insertion. In order to validate the obtained results, a comparison has been done with two other missions orbiting L1: ISEE-3 and ACE. Although the launch mass of SOHO is significantly larger than the other two missions, the comparison has been deemed to be reasonable, since the determining factor in the Tsiolkovsky equation is the mass ratio (MR).

Mission	$M_0[\text{kg}]$	$M_f[\text{kg}]$	MR	diff%
SOHO	1851	1602	1.1554	-
ISEE-3	479	390	1.2282	6.2985
ACE	757	562	1.3470	16.5777

Table 4: Comparison between missions

ISEE-3 is SOHO's predecessor mission, and for this reason has been the main inspiration for its design. Since the mission was the same, ISEE-3 performed a transfer trajectory and a halo orbit very similar to SOHO's one, in particular, the amplitude A_z of 120000 km is exactly equal to the one of the analyzed mission [6].

As a consequence, the values of the costs of the two MCCs ($\Delta v_{MCC1} = 17.9\text{ m/s}$, $\Delta v_{MCC2} = 24.8\text{ m/s}$) and the HOI ($\Delta v_{HOI} = 14\text{ m/s}$) manoeuvres can be considered as reliable estimates [4]. The total transfer manoeuvre cost amounts to a total of 56.7 m/s , which is, as expected, less than the Hohmann estimated budget since, in reality, such a transfer is studied to minimize the whole cost, in particular the HOI manoeuvre one.

For what concerns the SK, ISEE-3 performed very expensive manoeuvres compared to what is expected annually for this kind of orbits (30.06 m/s over four years [4]). In fact, pessimistic estimates of manoeuvre execution errors performed in pre-launch studies have shown that a typical SK manoeuvre cost would be $\leq 5\text{ m/s/year}$ [6]. This discrepancy is probably due to the fact that ISEE-3 has been the first S/C to ever orbit the L1 point and its technology was significantly less developed with respect to SOHO's.

ACE mission, on the other hand, was launched less than two years after SOHO and the station keeping technique is fundamentally the same [2]. For this reason, despite the difference in the operating orbit, it has been considered for the comparison of the SK manoeuvres. Taking into account the first eleven SK manoeuvres of ACE it emerges that the annual cost was $\approx 2.47\text{ m/s}$ [6].

2.2 Propulsion Architecture

The propulsion subsystem is one of the sub-assemblies of the SVM and its equipment is mounted onto the SVM upper platform except for two thruster blocks located on the lower floor.

The position of the thrusters has been carefully selected considering their plume impingement on experiments. A specific interface cylinder supports the propulsion tank and is connected on one side with the PLM internal cylinder and, on the other side, with the SVM thrust tube. The central positioning of the tank also allows to have a symmetric inertia matrix. The subsystem is a monopropellant blowdown propulsion system comprising a single large hydrazine fuel tank with helium as the pressurizing gas and a total of sixteen 4.5 N thrusters. The fuel, amounting to 251 kg at launch, is contained within a single oblate spheroidal tank that maintains separation between the hydrazine and its gaseous helium pressurant via a diaphragm, which also makes it possible to avoid sloshing.

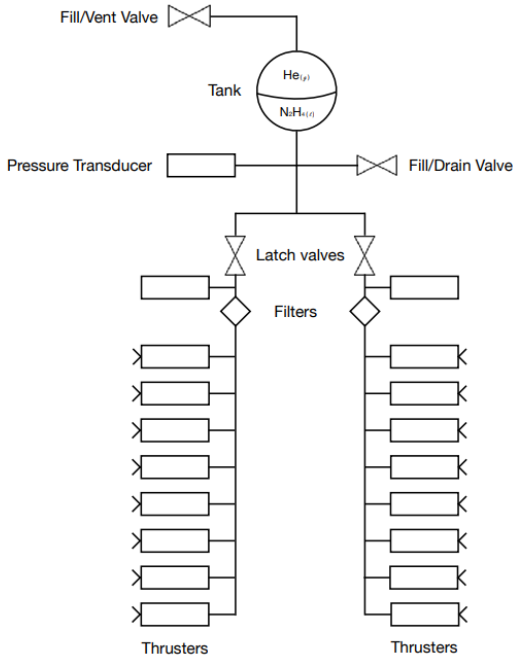


Figure 7: Propulsion subsystem architecture

The selected thrusters are the Northrop Grumman MRE-1.0 [8]:

MRE-1.0	
Propellant	Hydrazine
Specific impulse	220 s
Thrust at maximum pressure	4.5 N
Weight	0.5 Kg
Operating pressure range	3.45 - 27.58 bar
Thrust valve power at 28 VDC	8.5 W

Table 5: Thruster data

The sixteen thrusters are arranged into two fully redundant branches of eight thrusters, each providing both Δv and attitude control as needed.

The primary branch (A-branch) is used for commanded manoeuvres, while the redundant branch (B-branch) is used mainly in a hard-wired, emergency attitude control mode. The thruster configuration is the following:

Thruster Pair	Thruster Location	Δv Direction (body frame)	Primary Attitude Control	Thrust X_B -cosine	Thrust Z_B -cosine
1 and 2	Sunward	$-X_B$	Pitch	-0.866	+0.5 (1) -0.5 (2)
3 and 4	Earthward	$+X_B$	Yaw	+1	0
5 and 6	Top	$-Z_B$	Roll	0	-1
7 and 8	Bottom	$+Z_B$	Roll	0	+1

Table 6: Thrusters position and direction

As aforementioned, the chosen strategy for the feeding is a pressure-fed one. The volume of the tank from the datasheet is $V_{tank} = 0.461 m^3$ and statistically, these values lead to the choice of a pressure-fed pressurization system, as it is shown in Figure 8 [9].

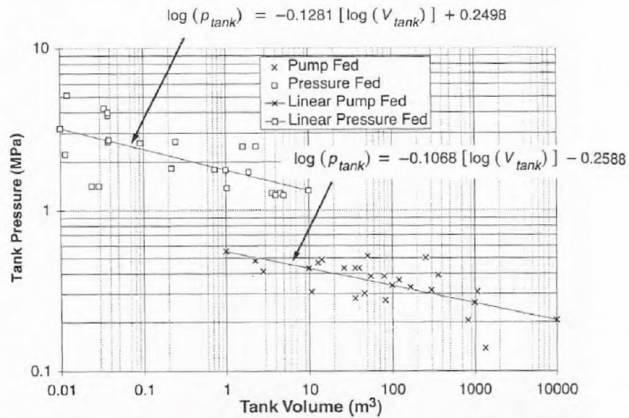


Figure 8: Pressure-fed vs Turbopump-fed

This solution is usually adopted when the tanks have a small size, while turbopumps are usually convenient only in the case of large tanks.

2.3 Reverse Sizing

2.3.1 Propellant and pressurizer selection

Among all the possibilities in terms of propellants, hydrazine (N_2H_4) is the preferred option, since it offers low density, high I_{sp} and is stable and insensitive to shock and friction.

In the selection of a pressurizing gas, the considered options included helium (He) and nitrogen (N_2), since they are both inert gases renowned for their non-reactive properties. Ultimately, helium was preferred over nitrogen due to its lower density, making it more conducive to the desired operational parameters.

2.3.2 Mass Breakdown

In order to obtain the propellant mass, it is needed to know the total dry mass of the S/C ($m_{dry} = 1602\text{ kg}$ [10]), the Δv ($237.6\frac{\text{m}}{\text{s}}$) from the mission design and the thrusters' specific impulse (Table 5).

Once this data are defined it is possible to invert the Tsiolkovsky equation to compute the mass ratio:

$$MR = \frac{M_0}{M_f} = e^{\frac{\Delta v}{I_{sp}g_0}} = 1.12 \quad (2)$$

And, consequently:

$$m_{in} = MR m_{dry} = 1788.44\text{ kg} \quad (3)$$

$$m_{prop,real} = 1.055 \cdot (m_{in} - m_{dry}) = 196.70\text{ kg} \quad (4)$$

A 5.5% margin³ has been added to the obtained m_{prop} value, in order to account for the ullage, the propellant residuals and the loading uncertainties.

Considering a propellant density of $\rho_{prop} = 1010\frac{\text{kg}}{\text{m}^3}$, the propellant volume reads:

$$V_{prop,real} = 1.1 \cdot \left(\frac{m_{prop,real}}{\rho_{prop}} \right) = 0.21\text{ m}^3 \quad (5)$$

An additional 10% margin is considered in order to take into account the unusable volume.

In order to size the system the value of initial pressure has been taken from literature [11], which is $P_{in} = 22\text{ bar}$. The final pressure has been computed by taking as a reference value the functioning pressure of the thruster at EOL ($P_{EOL} = 6.6\text{ bar}$) and adding the losses related to the injection (30% of the thruster operative pressure $\Delta P_{injection} = 0.3 \cdot P_{EOL} = 1.98\text{ bar}$) and feeding line ($\Delta P_{feed} = 50\text{ kPa}$) to it as follows:

$$P_f = P_{thruster} + \Delta P_{injection} + \Delta P_{feed} = 9.1\text{ bar} \quad (6)$$

It is then possible to compute the blowdown ratio as:

$$B = \frac{P_{in}}{P_f} = 2.42 \quad (7)$$

It is worth noting that this value falls short of the typical range. This decision might come from the aim to maintain a more consistent thrust and specific impulse throughout the S/C's lifespan. Opting for a

³All the values for the margins are taken from ECSS's directives

higher blowdown ratio could result in a more compact tank, but would also entail greater fluctuations in thrust levels during the mission.

In literature, the value for the final pressure and blowdown ratio are $P_f = 10 \text{ bar}$ and $B = 2.2$ which are similar to the ones computed.

Once these values have been settled, assuming that the expansion process follows an isothermal transformation the following relation holds true:

$$P_{in,He}V_{in,He} = P_{f,He}V_{f,He} \quad (8)$$

Then, knowing that:

$$V_{f,He} = V_{in,He} + V_{prop,real} \quad (9)$$

the initial volume occupied by the pressurizing gas:

$$V_{in,He} = \frac{V_{prop,real}}{B - 1} = 0.15 \text{ m}^3 \quad (10)$$

Since the initial pressure of the gas is known, it is possible to estimate its mass, assuming helium as a perfect gas, considering $T_{tank} = 293 \text{ K}$ and $R_{He} = 2077.3 \frac{\text{J}}{\text{kg K}}$:

$$m_{He,real} = 1.2 \cdot \left(\frac{P_{in,He}V_{in,He}}{R_{He}T_{tank}} \right) = 0.66 \text{ kg} \quad (11)$$

A 20% margin is added to the pressurizer mass as a convention.

For what concerns the propellant tank, two different metal alloys are usually considered: $Ti - 6Al - 4V$ and $Al7075$. For this mission $Ti - 6Al - 4V$ was selected, which is an alpha-beta titanium alloy with a high ultimate tensile strength and excellent corrosion resistance, even though it has a higher density with respect to $Al7075$.

Material	ρ	σ
Ti-6Al-4V	$4420 \frac{\text{kg}}{\text{m}^3}$	920 MPa
Al7075	$2810 \frac{\text{kg}}{\text{m}^3}$	503 MPa

Table 7: Materials properties

The tank is assumed to be a sphere as a first approximation and a 1% margin on the tank volume accounts for the presence of the diaphragm.

$$V_{tank,tot} = 1.01 \cdot (V_{prop,real} + V_{in,He}) = 0.37 \text{ m}^3 \quad (12)$$

$$r_{tank} = \sqrt[3]{\frac{3V_{tank,tot}}{4\pi}} = 0.44 \text{ m} \quad (13)$$

$$t_{tank} = \frac{P_{in}r_{tank}}{2\sigma} = 0.53 \text{ mm} \quad (14)$$

$$m_{tank} = \frac{4}{3}\pi\rho[(r_{tank} + t_{tank})^3 - r_{tank}^3] = 5.86 \text{ kg} \quad (15)$$

Eventually, the mass breakdown reads:

Tank	Pressurizer	Thrusters
5.87 kg	0.66 kg	8 kg

Table 8: Mass breakdown

Considering an additional 10% margin to account for the cables and miscellaneous the final mass of the propulsion system is:

$$m_{PS,real} = 1.1 \cdot (m_{tank} + m_{press,real} + 16 \cdot m_{th}) = 15.96 \text{ kg} \quad (16)$$

while the total amount of power requested from the subsystem:

$$P = n_{thruster} P_{thruster} = 136 \text{ W} \quad (17)$$

2.4 Comparison with the real system

It is now possible to compare the sizing with the real system data.

Comparison		
Parameter	Sizing	Real
m_{prop}	197 kg	251 kg
m_{tank}	5.87 kg	34.5 kg
V_{tank}	0.370 m^3	0.461 m^3

Table 9: Data comparison with real system

The difference in propellant mass is due to the different Δv , as explained in 2.1.4 and 2.1.5. This difference causes a consequent underestimation in the volume of the tank, since the estimated propellant mass is lower than the real one.

Lastly, the difference in mass is due to different reasons, such as taking the approximation of the tank as a sphere. Furthermore, the mass depends also on the tank thickness, which is estimated to be $t = 0.53 \text{ mm}$. This value is the minimum possible thickness to avoid breakage. More realistically, a safety factor could be taken into account, in order to increase this value, which would also allow an easier machining of the component.

3 Tracking, Telemetry and Telecommunication Subsystem

Change log	
§ 3.1	p.14: Specified downlink and uplink frequency bands
§ 3.3	pp.15-16: Added section
§ 3.4	p.16: Specified downlink and uplink conditions, added numerical results and adjusted bandwidth computation
§ 3.4.1	p.17: Added numerical results
§ 3.5	p.17: Added numerical results
§ 3.6	p.18: Modified section title and adjusted numerical results
§ 3.8	p.18: Added numerical results
§ 3.9	p.19: Added section
§ 3.10	p.20: Modified Table 11 and added Table 12

3.1 Architecture

The SOHO TTMTC architecture includes one High Gain Antenna (HGA) and two Low Gain Antennae (LGA), which both transmit in the S-Band, **respectively at 2245 MHz for downlink ($\lambda_{down} = 13.36 \text{ cm}$) and 2067 MHz for uplink ($\lambda_{up} = 14.51 \text{ cm}$)**. The receivers, transmitters and antennae are internally redundant or duplicated.

The HGA is a shallow reflector antenna, which receives both right and left circular polarized signals and is mounted on the floor of the SVM. Two stepper motors keep it pointed towards the Earth during the whole mission, tilting it of a $\pm 32^\circ$ angle. The dish has a diameter of 804 mm.

The two LGA are quasi-isotropic, quadrifilar, short resonant helix antennae, mounted on a short skirt. They are installed along the $+/- Z$ direction and they receive right circular polarized signals.

Additionally, a high-power amplifier (HPA), which is a solid-state amplifier, provides 10 (3.2) W output levels in its high (low) power mode.

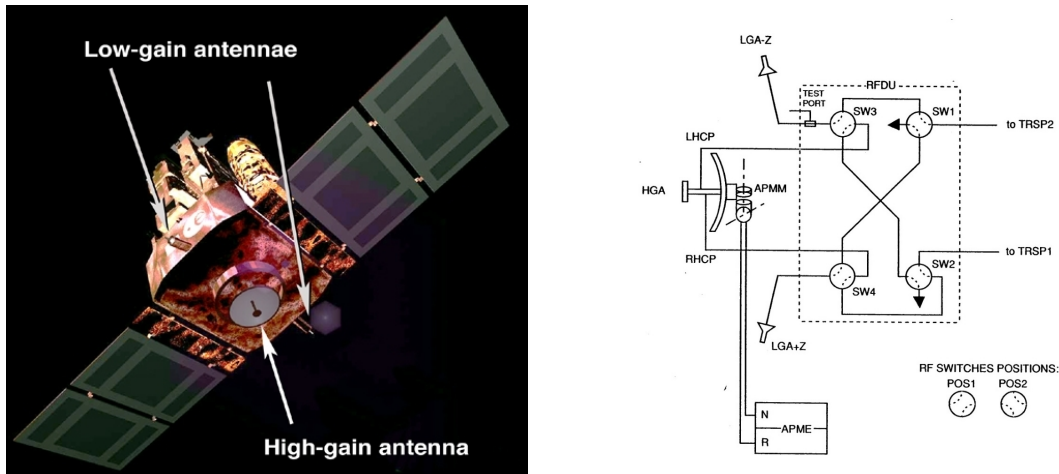


Figure 9: Antennae configuration

3.1.1 Configuration rationale

The presence of both an HGA and two LGA is justified by the need of communication both in non-nominal or uncontrolled phases (de-tumbling, unexpected ESR mode, etc.) and nominal operating situations. In the first case, the quasi-isotropy of the LGA is exploited and a weaker signal is accepted from any side of SOHO, while in the latter situation the HGA guarantees a continuous and powerful signal transmission, suitable for the downlink of all the telemetry and scientific data acquired by the P/L.

The communications with the ground stations are accomplished with the 26 m and 34 m antennae of the NASA DSN in Goldstone (CA), Madrid (ESP) and Canberra (AUS).

The SOHO S/C utilizes the ESA standard packet telemetry structure. Each transfer frame is composed of 1279 bytes, including the Reed-Solomon (R-S) code. Both R-S and convolutional encoding are used for the downlink data, allowing the signal to achieve the desired BER with a low Eb/N0.

3.2 Time windows and phases

During the main phases of the mission, different solutions for the communications have been selected:

- **Launch and Early Orbit Phase:** no communication with the ground is foreseen during this phase.
- **Transfer Trajectory Phase:** from the injection of the S/C into the transfer orbit (MECO2) until its injection into the halo orbit, housekeeping and science telemetry, telecommand, and ranging links are established. After the first three days of continuous contact with the GSs, the normal operations contact sequence begins. This latter scenario is based on three daily passes of 1.6 h each and one 8 h pass, as during the normal halo-orbit phase. However, the ground segment will be continuously available for critical support.
During the LR subphase, the redundant low-gain antennae are both available for the low data rate only, while during the HR subphase, the high-gain antenna should be deployed, providing both uplink reception and medium- or high-rate telemetry downlinking for the remaining part of the TTP and successive operative mission conditions.
- **Halo-Orbit Phase:** during the nominal phase of the mission, three daily passes of 1.6 h and one 8 h pass are scheduled for SOHO support during 10 months per year, the remaining 2 months having full 24 h/day support. The onboard data recorder provides data storage during all non-contact periods. These contacts are sufficient for complete recorder-play-back data capture and to meet all telemetry, ranging and command requirements. During the operational phase, any combination of the ranging, telemetry, and telecommanding links will nominally be available.

In particular, the communication windows for the Halo Orbit Phase have to be clarified.

Theoretically, due to the L1 halo orbit followed by SOHO, it would be possible to communicate with the GSs in a continuous and permanent way (i.e. 24h/day). However, due to the following issues, the former strategy has been substituted by a multiple-time window communication approach:

- Low-quality communication when the S/C's elevation angle is under a certain level, due to high atmospheric signal losses
- Necessity of continuous incoming scientific data only during experimental campaigns, that is not the whole year time period
- Possibility for the GS antennae to communicate also with other S/Cs

3.3 Encoding and Modulation

The modulation and encoding techniques adopted on the SOHO S/C are, respectively, QPSK modulation ($\alpha_{mod} = 2$) and both Reed-Solomon and convolutional encoding ($\alpha_{enc} = 2$).

For what concerns QPSK, among the traditional phase modulation methods, filtered QPSK is the most bandwidth-efficient. QPSK modulation has been used over the years for medium and high telemetry data rate transmissions. Viewed as two orthogonal BPSK/NRZ channels, QPSK bit-error-rate performance is equal to that of BPSK/NRZ with half of the data rate on each channel. Like all suppressed carrier systems, a somewhat higher Costas loop SNR is required for proper operation than in the case of a residual carrier phase-locked loop.

QPSK, coupled with a Butterworth filter, has been the modulation method of choice for medium and high data rate missions due to its appreciable performances in terms of power containment percentage

[12, pp.34-38][13, p. 127].

Regarding the encoding, the Reed-Solomon code may be used alone, and as such it provides an excellent forward error correction capability in a burst-noise channel. However, should the Reed-Solomon code alone not provide sufficient coding gain, it may be concatenated with the convolutional code. Used this way, the Reed-Solomon code is the outer code, while the convolutional code is the inner one [14, pp. 26-37].

Since the ratio between the α coefficients corresponding to the selected techniques for encoding and modulation evens out, the data rate remains unchanged. In particular $R_{down} = 405.8 \text{ kbps}$ (science + TM) [15] have been considered for the downlink and $R_{up} = 4 \text{ kbps}$ (TC + TM) [16] for the uplink, both being considered for the worst case scenario.

3.4 SNR and Link Budget

Throughout this paper, two different situations, being considered the most significant ones in terms of TMTTC subsystem, have been analysed. The first one is a downlink condition, carried out using the HGA and typical communication strategy in the nominal phase. As for the second one, a situation in which the LGA is used has been sought. In particular, uplink during the safe mode, during which the possibility of sending commands to the S/C is essential, has been analysed.

The aim of this section is to obtain an estimation of the input power, analyzing a downlink situation where the high gain antenna (HGA) of SOHO communicates with the 26 m antenna of the NASA's DSN ($D_{rx} = 26 \text{ m}$). However, the steps and formulas are the same for the uplink condition. In order to size the subsystem properly, the worst case scenario has been considered, characterised by the maximum value of data rate to be transmitted.

The approach starts from the assumption of the minimal acceptable signal to noise ratio (SNR). Considering a 3 dB margin and given that the minimum SNR value requested by the DSN is 10 dB:

$$SNR_{margin} = SNR_{carrier} - SNR_{minimum} \geq 3 \text{ dB} \quad (18)$$

from which a $SNR_{carrier} = 13 \text{ dB}$ is obtained.

Subsequently, the carried power is computed:

$$P_{carrier} = SNR_{carrier} + N_0 + 10 \log_{10} (B) = -141.52 \text{ dBW} \quad (19)$$

being the bandwidth $B = R_{down} (1 + \alpha_{mod}) = 1.2174 \text{ kHz}$ and the system noise density

$$N_0 = 10 \log_{10} (kT_s) = -215.38 \text{ dB} \quad (20)$$

where $k = 1.38 \cdot 10^{-23} \frac{W_s}{K}$ is the Boltzmann's constant and T_s is the sensor's temperature. In particular, this temperature is set to 21 K for the DSN[17].

Once the carried power has been computed, the actual received power by the DSN can be obtained, considering the power losses due to modulation:

$$P_{rx} = P_{carrier} - P_{mod,loss} \quad (21)$$

where

$$P_{mod,loss} = 20 \log_{10} (\cos (\beta)) = -4.83 \text{ dBW} \quad (22)$$

being β the modulation index of the receiver, assumed to be equal to 55°.

From Equation 21, $P_{rx} = -136.70 \text{ dBW} = 2.14 \cdot 10^{-17} \text{ kW}$ can be obtained, which is coherent to the value that can be found on the Deep Space Network Website: 10^{-17} kW [18].

From the Link Budget Equation, it is now possible to compute how much power has to be generated from SOHO in order to achieve the desired parameters values during the communication link.

$$P_{tx} = P_{rx} - G_{tx} - G_{rx} - L_{space} - L_{atmospheric} - L_{cables} - L_{pointing} \quad (23)$$

All the remaining unknown values are computed in the following section.

3.4.1 Gain and losses calculation

The gain of the High Gain Antenna of SOHO has been estimated considering the following formula, with $\mu_{parabolic} = 0.55$, $\lambda = 13.36 \text{ cm}$, $D = 804 \text{ mm}$.

$$G_{HGA} = G_{tx} = 10 \log_{10} \left(\frac{\pi^2 D^2 \mu_{parabolic}}{\lambda^2} \right) = 22.93 \text{ dB} \quad (24)$$

On the other hand, the gain of the DSN antenna has been considered to be 52.18 dB [16].

Regarding the signal losses, the following loss sources have been considered:

$$L_{pointing} = -12 \left(\frac{\eta}{\theta_{rx}} \right)^2 = -3.25 \cdot 10^{-6} \text{ dB} \quad (25)$$

$$L_{space} = \left(\frac{4\pi r}{\lambda} \right) = -223 \text{ dB} \quad (26)$$

where $\eta = 0.01^\circ$ is the pointing accuracy of the DSN, $\theta_{rx} = \frac{65.3\lambda}{D_{rx}} = 0.3356 \text{ rad}$ is the receiver beamwidth and $r = 1.5 \cdot 10^6 \text{ km}$ is the L1-Earth distance, taken as reference value for the nominal orbit.

In addition, the cable losses value L_{cables} has been selected in a range between -1 dB and -3 dB as -1 dB and the signal attenuation due to the presence of the Earth atmosphere has been set to be $L_{atmospheric} = -0.21 \text{ dB}$ [16].

From Equation 23, the power transmitted results: $P_{tx} = 12.39 \text{ dBW} = 17.33 \text{ W}$.

As a final check, both the EIRP and the Eb/N_0 values have been computed:

$$EIRP = P_{tx} + G_{tx} + L_{cables} = 34.32 \text{ dBW} \quad (27)$$

$$\frac{Eb}{N_0} = P_{rx} - N_0 - 10 \log_{10} (R_{down}) = 22.60 \text{ dB} \quad (28)$$

which are coherent with the usual margins considered for these parameters and higher than the minimum values associated to a $BER = 10^{-5} \div 10^{-7}$.

3.5 Transmitted and input power and amplifier selection

The transmitted power can be obtained from Equation 23 and it amounts to $P_{tx} = 12.39 \text{ W}$. The satellite is equipped with a solid state amplifier (SSA) and, from Figure 10, knowing that the output power equals the power transmitted, the input power can be retrieved, which results in $\approx 50 \text{ W}$. This leads to a design of a SSA with an efficiency of about 20% .

This value represents the main component of the power budget of the TTMTTC subsystem with few other minor contributions that have been neglected as a first approximation. This last assumption is supported by the considered margins, broader than the actually adopted ones.

Regarding the mass budget, the advantage of a SSA is its inherent light weight, substantially less than a TWTA for low power outputs like the ones that are required in this case.

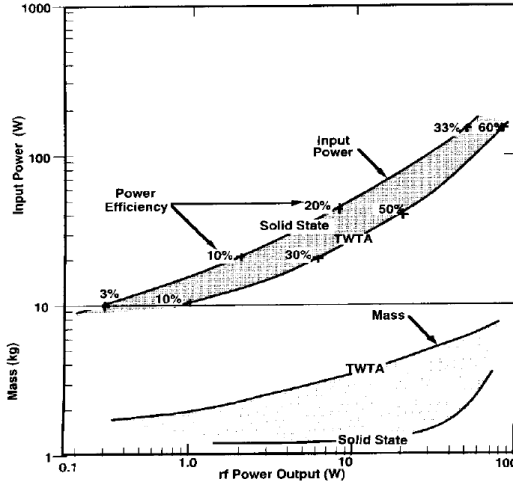


Figure 10: Amplifier efficiency

T NUOVO N0?

3.6 Uplink communications during Safe Mode

In this section, a brief discussion about uplink transmission and communication through the LGA is carried out.

Considering an uplink communication condition between SOHO's LGA and DSN's 26 m antenna, the computational approach has been the same as the downlink condition analysed in Section 3.4. The main concepts that have been pursued are the following:

- A different adopted value of the data rate, here considered to be $R_{up} = 4 \text{ kbps}$ ($B = 12 \text{ kHz}$) as a telemetry-only worst case scenario
- A slightly higher SNR_{min} value, estimated as 15 dB in order to take into account the greater difficulty to distinguish the incoming signal from the noise, both for the different architectures between the DSN antenna and the LGA and for the higher noise
- The same losses values, apart from the ones depending on the signal frequency (L_{space} and $L_{pointing}$), which have been corrected with the uplink frequency value

All the significant results are reported in Section 3.9.

3.7 Data volume

As previously mentioned in Section 3.2, the nominal communication to the ground happens in different time windows, spread along the day. From [18], it has been observed that, for the downlink communication, a rather constant data rate of 245.8 kbps is maintained.

Regarding the data volume computation, during the two month 24h communication reads;

$$60 \text{ d} \cdot 24 \text{ h} \cdot 60 \text{ min} \cdot 60 \text{ s} \cdot 245.8 \text{ kbs} = 1.27 \text{ Tb} \quad (29)$$

while, for the remaining days:

$$305 \text{ d} \cdot 12.8 \text{ h} \cdot 60 \text{ min} \cdot 60 \text{ s} \cdot 245.8 \text{ kbs} = 3.44 \text{ Tb} \quad (30)$$

Resulting in a total annual data volume of 4.71 Tb .

As for the uplink communication, the telecommands data rate has been found equal to 4 kbps . Since this type of data is generally sent during the 1.6 hours windows and it has been assumed that the data volume does not change during the 24/7 communication:

$$365 \cdot d \cdot 1.6 \text{ h} \cdot 60 \text{ min} \cdot 60 \text{ s} \cdot 4 \text{ kbps} = 8.4 \text{ Gb} \quad (31)$$

3.8 Channel capacity verification

The Shannon–Hartley theorem states that:

$$C = B \log_2 \left(1 + \frac{P_{rx}}{N} \right) = 7.24 \cdot 10^3 \text{ kbps} \quad (32)$$

$$N = kT B = 3.53 \cdot 10^{-16} \text{ W} \quad (33)$$

where C is the channel capacity and N is the noise, considering downlink ($T = 21 \text{ K}$). The channel capacity is the maximum possible data rate that can be theoretically reached by the system. In the worst case scenario a data rate of 405.8 kbps has been considered (telemetry + science data), assuming convolutional encoding and QPSK modulation coefficients of SOHO's equipment both equal to 2. Since this value is far lower than the aforementioned channel capacity, the saturation condition is not reached.

3.9 Results

The following table summarizes the obtained results both for the downlink and uplink transmissions.

	Downlink	Uplink
G_{ant} [dBi]	22.93	-11
L_{pointing} [dBW]	$-3.25 \cdot 10^{-6}$	$-2.75 \cdot 10^{-6}$
L_{space} [dBW]	-223	-222.27
P_{carrier} [dBW]	-141.52	-145.83
N_0 [dB]	-215.38	-204.62
N [W]	$3.53 \cdot 10^{-16}$	$4.14 \cdot 10^{-17}$
P_{rx} [dBW]	-136.70	-141.00
P_{rx} [kW]	$2.14 \cdot 10^{-17}$	$7.94 \cdot 10^{-18}$
P_{tx} [dBW]	12.39	41.30
P_{tx} [W]	17.33	$1.35 \cdot 10^4$
EIRP [dBW]	34.32	92.48
E_b/N_0 [dB]	22.60	27.60
C [kbps]	$7.24 \cdot 10^3$	91.09

Table 10: Downlink and Uplink numerical results

3.10 Conclusions and comparison

In this final section, a comparison between the computed results and the actual data [16] regarding the Link Budget Equation is presented. [Table 11 and Table 12 display, for both the conditions](#), how the computed values present slim discrepancies from the real ones, as corroboration of the method adopted in the previous sections. It is important to keep in mind that the actual data are taken from the worst case scenario.

	Transmitted Power [dBW]	Gain of HGA [dBi]	L_{pointing} [dBW]	L_{space} [dBW]	EIRP [dBW]
Real data	10	21.10	0	-224.07	27.22
Computed results	12.39	22.93	$-3.25 \cdot 10^{-6}$	-223	34.32

Table 11: Comparison with real data for downlink configuration

	Transmitted Power [dBW]	Received Power [dBW]	L_{pointing} [dBW]	L_{space} [dBW]	EIRP [dBW]
Real data	39.50	-116.47	0.20	-233.35	90.10
Computed results	41.30	-141.00	$-2.75 \cdot 10^{-6}$	-222.27	92.48

Table 12: Comparison with real data for uplink configuration

Since all the computed link budget terms are very similar to what it is reported in the literature about SOHO and since the whole estimation starts from the assumption of the minimum SNR, it is possible that the SNR_{minimum} of $10\ dB$, usually used for deep-space missions, with distances a few orders of magnitude larger than the one between SOHO and the Earth, is too conservative.

4 Attitude and Orbit Control Subsystem

4.1 Architecture

SOHO is a 3-axis stabilized S/C. The AOCS aims to provide the satellite with the means to:

- Point the S/C optical reference axis X_0 accurately to the Sun
- Control the roll angle around the Sun pointing axis
- Perform orbit manoeuvres

The mission requirement is to maintain the attitude such that the solar spin axis is contained in the X_B - Z_B plane as the spacecraft proceeds around the Sun. This results in the spacecraft rolling between approximately $\pm 7.25^\circ$ over the course of a year [1].

In order to understand the direction of the sensors, the five mainly used reference frames shall be defined.

- S/C body axes X_B, Y_B, Z_B
- S/C optical axes X_0, Y_0, Z_0
- Payload interface frame X_{pi}, Y_{pi}, Z_{pi}
- Inter-instrument X_{ii}, Y_{ii}, Z_{ii}
- Absolute attitude frame X_a, Y_a, Z_a

The S/C optical axes are defined with respect to the optical alignment cube of the Fine Pointing Sun Sensor (FPSS), with the optical X-axis (X_0) nominally perpendicular to the S/C launcher separation plane and pointing from the separation ring through the spacecraft. The X_0 -axis is the reference axis of the FPSS measurements. The optical Y-axis (Y_0) is along the direction of the solar panel extension with positive Y_0 pointing from the interior towards the UVCS instrument. Z_0 completes the right-handed orthogonal frame.

Nominally, the optical RF is such that the axes are parallel to the S/C body axes (X_B, Y_B, Z_B).

The AOCS comprises the following sensors and actuators (mass and power budgets are reported per unit component):

Sensors and Actuators	Quantity [-]	Weight [kg]	Power [W]
Fine Pointing Sun Sensor (FPSS), aligned with the optical X axis (X_0) [19]	2	0.95	-
CCD-based Star trackers, comprising the Star Sensor Unit (SSU) [20]	2	7.2	-
Rate-Integrating Gyros (Inertial Reference Unit, IRU) [15]	3	-	-
Reaction Wheels, pyramidal configuration [21] Hydrazine Thrusters [8]	4 (3 + 1) 16 (8 + 8)	29.8 8	504 68

Table 13: On-board sensors and actuators

The thrusters are utilized for momentum unloading and orbit adjustments as well as attitude control in early transfer trajectory.

During the Halo phase, in nominal fine pointing mode, the S/C performances are set as follows (3σ values):

- **Absolute Pointing:** The S/C optical X-axis (X_0) pointing towards the photometric centre of the Sun and the S/C optical Z-axis (Z_0) oriented towards the north ecliptic hemisphere, such that the ($X_0 - Z_0$) plane contains the Sun axis of rotations. Y_0 will be parallel to the solar equatorial plane pointing towards the east. The maximum APE of the X_{pi} axis from on-ground alignment

until the end of the nominal mission shall be less than 5 arcmin. The maximum variation of the APE of the roll angle about the X_a axis shall be less than 15 arcmin.

- **Relative Pointing Errors:** The medium-term APE of the X_{pi} axis shall be less than 10 arcsec over a time period of 6 months. The relative short-term pointing error shall be less than 1 arcsec over a time period of 15 minutes. The short-term roll error about the X_a axis shall be less than 1.5 arcmin, also over a time period of 15 minutes.

4.2 Design rationale

The spacecraft pointing requirements and performance [22] are given as:

Absolute Pointing Accuracy	10 arcsec
Relative Pointing Accuracy	1 arcsec in 15 min
Absolute Roll Accuracy	15 arcmin
Relative Roll Accuracy	1.5 arcmin in 15 min
FPSS Initial Calibration Accuracy	5 arcsec
Attitude Control Error	1 arcmin
Potential Experiment Misalignment (in flight)	4.5 arcmin
Potential Misalignment Drift	12 arcsec per year

Table 14: Pointing and Alignment Parameters

Since the mission is designed to constantly monitor the solar activity far from the Earth, the selection of FPSSs seems a logical choice, paired with a set of two star sensors. This last couple of sensors is adopted to fulfill the stringent pointing requirements and they are positioned on one of the surfaces not directly exposed to the Sun under nominal condition, in order to preserve the sensitive optics. The star sensors acquire the positions of a set of stars in a direction roughly orthogonal to the Sun, making it possible to determine the attitude of the S/C. Moreover, this set of measurements, along with the angular velocities retrieved by the set of gyroscopes, are sufficient to fully determine the state vector describing the kinematics and dynamics of the S/C.

The functioning of the aforementioned sensors is guaranteed during both the nominal and the transfer phases, since the S/C is always maintained with the X_B axis pointing towards the Sun and it is spinning around the same axis to guarantee better stability in case of correction manoeuvres.

The attitude sensors are installed on the PLM, in order to achieve the highest possible alignment stability, and they are duplicated to guarantee the required redundancy.

In order to transfer high-rate data, SOHO needs to always have a way to align the HGA with the ground stations. Since the pointing requirements of the antenna would clash with the requirements of the P/L, the antenna has been provided with the capability of tilting of $\pm 32^\circ$ via two stepper motors. In this way both the pointing requirements for the P/L and TMTC can be satisfied.

The satellite is controlled by a closed-loop control system, exploiting a system of four reaction wheels that enable the S/C to reach the pointing accuracy demanded mainly by the scientific instruments on board. Necessary desaturation manoeuvres are managed by a set of eight couples of mono-propellant cold-gas thrusters, positioned on the SVM to avoid having thruster plume impingement on science instruments. These same actuators are used to perform periodical SK corrections, that are often performed in a conjunct manner with the desaturation manoeuvres, in order to lower the cost in terms of propellant and promptly intervene in case of unwanted perturbations caused by unbalanced forces. Moreover, the addition of a fourth RW and having pairs of thrusters ensures redundancy in the control, that is clearly one crucial requirement in the design of a spacecraft which has to survive for an extended period of time in an harsh environment.

4.3 Control Modes

The following main modes are defined for the SOHO S/C:

- Inactive
- Standby
- Initial Sun Acquisition (ISA)
- Roll Maneuver Wheels
- Fine Sun-pointing Acquisition (FSA)
- Coarse Roll pointing
- Normal
- Emergency Sun Reacquisition (Safe mode)

Immediately after SOHO's separation from the Centaur upper stage, the AOCS will cancel the angular rates imparted by the separation and will coarsely align the S/C towards the Sun, using hydrazine thrusters and Sun-acquisition sensors, arranged in a configuration giving omnidirectional coverage. The control algorithms reside in the memory of an onboard microprocessor that processes the sensor data and issues commands to the thrusters.

SOHO's solar panels will be deployed with the AOCS in standby configuration [23].

After full deployment of the solar panels has been achieved, the AOCS will again coarsely point the spacecraft at the Sun and perform the transition to fine Sun pointing and roll-angle control using a FPSS, a star tracker and three reaction wheels. Once this configuration has been achieved, the payload instruments will start making their scientific observations, when the spacecraft's pointing towards the Sun is stabilised to within a few tenths of an arcsecond under quiescent conditions (i.e. when no spacecraft or experiment mechanism is being operated) or within about one arcsecond when some mechanisms are active to realign the HGA or to adjust an experiment's line of sight.

Among the aforementioned modes, the most critical ones, linked to the recovery of the nominal attitude after an emergency, are described in the following sections [24].

4.3.1 Normal Mode (NM)

In NM, the attitude is controlled by spinning up or slowing down three RW, oriented in a triangular fashion to each other (pyramidal configuration, that allows a lower request of momentum from the control system). The inputs to the control algorithm come from the Fine Pointing Sun Sensor (FPSS) and a star tracker, a small telescope oriented 90° away from the Sun. The "Roll Steering Law" (RSL) dictates the movement of the stars in the star tracker to keep SOHO oriented exactly in line with the Sun's North-South axis.

4.3.2 ESR Mode (Emergency Sun Reacquisition)

In ESR, the spacecraft attitude is controlled entirely by hardware that senses the approximate position of the Sun and fires thrusters autonomously to ensure that the spacecraft is pointing towards that direction ($\pm 2^\circ$ on each axis). The spacecraft roll is not controlled by the hardware, but it can be controlled by ground intervention.

The reaction wheels are not autonomously activated by the S/C, so they progressively slow down, imparting an angular momentum on the rest of the spacecraft, which is counteracted by the thrusters firings once the pointing reaches a 2° error limit. After the wheels are slowed down, the spacecraft pointing remains within a $2^\circ \times 2^\circ$ error box.

However, through ground intervention, the reaction wheels can be spun up, making them provide gyroscopic stability to the S/C. When tuned correctly, the spacecraft can be left in ESR mode with wheels spun up with practically no thruster firings.

In this mode, the High Gain Antenna (HGA) cannot be used, because of the inaccurate Earth-pointing. Instead, the two omnidirectional Low Gain Antennae (LGA) are used to transmit vital information to ground controllers.

ESR mode can be triggered by a number of "safety features". The trigger has typically been the so-called Fine Sun Pointing Attitude Anomaly Detector (FSPAAD). This is entirely independent of the AOCS and is supposed to trigger when the Sun is outside a 5° radius error circle. There is also a similar sensor called the CSPAAD (Coarse SPAAD) that triggers at a 25° radius error circle.

When ESR is triggered, an alert message is sent to most of the instruments in order to turn them off, if necessary. The reason is that some instruments do not tolerate even minimal deviations from the correct attitude without incurring damage (e.g. LASCO, which blocks out direct sunlight with an occulter, would quickly overheat if the Sun was suddenly let shining directly onto the sensor part of the instrument). Furthermore, some instruments are very sensitive to contamination from thrusters' firing (e.g. CDS, SUMER, CELIAS/STOF). Even if EIT is not directly affected by a loss of nominal attitude, since it shares its electronics box with LASCO, its instruction queue is supposed to get flushed as a result of an ESR flag.

4.3.3 CRP Mode (Coarse Roll Pointing)

In this mode, the first step after ESR, only the reaction wheels are used for attitude and roll control. Pitch and yaw are determined through the FPSS, and the roll rate is measured with the gyroscopes.

In CRP, SOHO can be commanded to point correctly at the Sun, and it is stable enough to do a star mapping through the star tracker, so the absolute roll can be determined through the reaction wheels. It can then be commanded to roll back to near nominal roll orientation, and the HGA can be re-oriented towards Earth.

4.3.4 RMW Mode (Roll Maneuver Wheels)

In RMW, the intermediate mode between CRP and Normal Mode, SOHO is controlled by the FPSS and the star tracker. In other words, SOHO has full knowledge and control of its orientation. However, the steering laws are a bit more "relaxed", and a strict alignment with Solar North-South is not maintained. This mode is used for thruster manoeuvres: Station Keeping (SK) manoeuvres, which are used to trim SOHO's orbit, and Momentum Management (MM) manoeuvres, that allow reaction wheels' desaturation when necessary. The wheel speeds must be kept within certain ranges to maintain stable control.

4.4 Sizing

In this section a preliminary sizing of the actuators is presented, considering the worst case during normal mode. This follows an estimation of the overall S/C's mass distribution and the main disturbances and manoeuvres that SOHO should be capable of facing during its operating lifetime.

Both the actions have been attributed to the reaction wheels, which are then properly desaturated using the thrusters.

The data for the reaction wheels, taken from [21], are reported below.

#	4
h_{max} [Nm]	45
ω_{max} [RPM]	4000
M_{max} [Nm]	0.265
Dimensions [mm]	\varnothing 365 x 125
Mass [kg]	7.45
Peak power [W]	168

Table 15: RW data

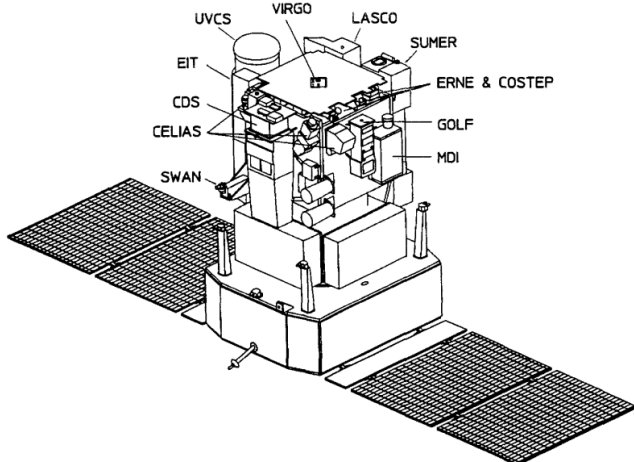
4.4.1 Inertial properties

In order to properly exploit the $\{X_B, Y_B, Z_B\}$ reference frame, the position of the S/C's barycenter (c_g) has been computed, given the following overall mass distribution: $m_{PLM} = 650 \text{ kg}$, $m_{SVM} = 1095 \text{ kg}$ and $m_{panel} = 52.5 \text{ kg}$.

Given these data, the obtained position of the c_g along the X_B -axis is about 17 cm below thrusters 5, 6, 7, 8, while on the other axes a symmetric mass distribution has been assumed in the first place, thus locating the barycenter in the middle of the respective axes⁴ and resulting in the following inertia matrix:

$$\mathbf{I} = \begin{bmatrix} I_{roll} & 0 & 0 \\ 0 & I_{pitch} & 0 \\ 0 & 0 & I_{yaw} \end{bmatrix} = \begin{bmatrix} 977.43 & 0 & 0 \\ 0 & 1232.91 & 0 \\ 0 & 0 & 2210.33 \end{bmatrix} [\text{kg m}^2] \quad (34)$$

The actual barycenter location along the Y_B and Z_B axes is dictated by the weight and positions of the main scientific payloads. The information that has been found are summarized in the following table:



Payload	Weight [kg]
CDS	100
SWAN	13.25
MDI	56.5
SUMER	77.1
UVCS	120
ERNE	9.3
VIRGO	14.5
COSTEP	9.2
LASCO	25

Table 16: Payloads weights

Figure 11: Payloads disposition

From both Figure 11 and Table 16 it can be noticed that the weight of CDS is counter-balanced by LASCO and SUMER, placed on the opposite face. On the other hand, UVCS (which is the heaviest instrument on board and the most dislocated from the center) presumably is not completely counterbalanced by the instruments on its opposite direction. For this reason, the position of c_g in the $Y_B - Z_B$ plane can be assumed to be shifted towards UVCS.

4.4.2 Disturbances

Disturbances are a crucial issue to deal with during a mission in space and they can be subdivided into internal and external.

Several different types of internal disturbances are present in a real satellite environment, spacing from uncertainties on center of mass's position to thrusters' alignment and more complex structural and dynamical behaviors. Being this report focused on nominal performances, the mentioned internal disturbances will not be accounted for henceforth.

⁴Due to the assumed symmetry of the masses with respect to the X_B -axis in a nominal Sun-pointing situation like the one considered in Section 4.4.2, the corresponding disturbance due to SRP would result in a 0 Nm torque on the S/C. Being the Sun Radiation Pressure the main source of disturbance in a L1 halo orbit, it is clearly contradictory not to consider it

For what concerns the external sources of disturbance, since the S/C is orbiting at L1, the main external disturbance considered is the SRP, which has been taken into account with the following data, valid for the worst case scenario:

$F_s = 1367 \text{ W} \cdot \text{m}^{-2}$	Solar constant at Earth
$c = 300000 \text{ km} \cdot \text{s}^{-1}$	Speed of light
$A_s = 34.675 \text{ m}^2$	S/C surface facing the Sun
$q = 0.3$	Reflectivity coefficient
$I = 0^\circ$	Incidence angle
$(c_p - c_g)$	Distance between the satellite c_p and c_g

Table 17: Solar pressure data

$$M_{SRP} = \frac{F_s}{c} A_s (1 + q) \cos(I) (c_p - c_g) \quad (35)$$

However, with the considerations made in Section 4.4.1 on the barycenter position and being the center of pressure (c_p) assumed to be located in the middle of the $+X_B$ facing surface, it is not possible to compute a meaningful value for M_{SRP} . In order to avoid this issue, a 10^{-5} Nm order of magnitude has been considered, accordingly with literature data [25], thus obtaining a 4.87 cm c_g displacement on the aforementioned surface towards UVCS.

4.4.3 SRP compensation

Being the center of mass shifted along the positive direction of the pitch axis, the corresponding SRP-disturbance torque is generated around the negative direction of the yaw axis and the control torque shall compensate this rotation.

Knowing that the period of the halo orbit is $t_{orbit} = 178$ days, the angular momentum stored by a single reaction wheel every orbit can be computed as follows:

$$h_{RW,stored} = M_{SRP} t_{orbit} = 307.58 \text{ Nms} \quad (36)$$

where a 100% margin has been considered on the disturbance torque value. Being the maximum angular momentum storage $h_{max,RW} = 45 \text{ Nms}$, the fraction of orbit, decreased by a 20 % margin, in which the wheel reaches its saturation condition is:

$$n_{orbit,sat} = 0.8 \frac{h_{max}}{h_{RW,stored}} = 0.117 \quad (37)$$

which corresponds to a $20 \text{ d } 20 \text{ h}$ period.

In order to desaturate the reaction wheels the disturbance torque has to be countered. The usage of thruster $n^o 4$ guarantees a moment around the positive yaw direction, even if it also introduces an unbalanced force in the system⁵. The orbit perturbation due to this force is not considered here for simplicity's sake.

In the absence of further constraints for this manoeuvre, the thruster exploits its maximum achievable thrust ($T_{th} = 4.4 \text{ N}$), resulting in a desaturating torque $M_{th,desat} = R_{3,4} T_{th} = 3.08 \text{ Nm}$. The needed time for complete desaturation then is:

$$t_{desat,SRP} = \frac{h_{max}}{M_{th,desat}} = 14.61 \text{ s} \quad (38)$$

⁵The thrusters' configuration is reported in the Appendix A.

which can be considered a realistic and feasible time period.

Finally, given that the considered upper bound for the mission to last was $t_{mission} = 6 \text{ years} \approx 2190 \text{ days}$, the total mass of propellant needed for desaturation of the 3 reaction wheels during SRP compensation reads:

$$m_{prop,SRP} = 3 \frac{t_{desat,SRP} T_{th}}{I_{sp} g_0} n_{desat,SRP} = 9.47 \text{ kg} \quad (39)$$

where $n_{desat,SRP} = \left\lceil \frac{t_{mission}}{t_{orbit}} \frac{1}{n_{orbit,sat}} \right\rceil = 106$ is the number of times in which the desaturation is required during the whole mission.

4.4.4 Slew manoeuvre

The worst case scenario for a slew manoeuvre, consisting in a half rotation ($\theta_{slew} = 180^\circ$) around the maximum inertia axis I_{yaw} , is considered hereafter (see Equation 34).

Furthermore, the maximum sustainable slew angular rate is imposed by the sensor that requires the highest stability for its functioning. In this case the star tracker has been selected as the most crucial one ($\omega_{slew,max} = 0.5^\circ/\text{s}$), thus setting the minimum achievable time for the slew to $t_{min,slew} = \frac{\theta_{slew}}{\omega_{slew,max}} = 360 \text{ s}$.

Assuming that the manoeuvre consists of an acceleration phase and a breaking one, both with the same time duration and angular acceleration, the requested torque and angular momentum read:

$$M_{slew} = 4 \theta_{slew} \frac{I_{yaw}}{t_{min,slew}^2} = 0.214 \text{ Nm} \quad h_{slew} = M_{slew} t_{min,slew} = 77.16 \text{ Nms} \quad (40)$$

Since the overall requested torque does not exceed the maximum reachable value of the reaction wheels ($M_{max} = 0.265 \text{ Nm}$), the manoeuvre can be performed in the minimum possible time $t_{min,slew}$.

The desaturation procedure using the thrusters is completely analogous to the one presented in Section 4.4.3. Using in this case one of the thruster between $n^\circ 3$ and $n^\circ 4$ in an arbitrary way, considering the maximum thrust and the angular momentum requested by the slew manoeuvre:

$$t_{desat,slew} = \frac{h_{max,slew}}{R_{3,4} T_{th}} = 25.05 \text{ s} \quad (41)$$

which eventually leads to the definition of the needed propellant mass for each manoeuvre to be performed with complete wheels' desaturation:

$$m_{prop,slew} = 3 t_{desat,slew} \frac{T_{th}}{I_{sp} g_0} = 0.15 \text{ kg} \quad (42)$$

4.5 Conclusions

The SOHO mission was designed such that the allocated Δv for attitude control is $\Delta v_{att} = 43 \text{ m/s}$. Furthermore, the sum of the HOI manoeuvre and the two MCCs manoeuvres leads to $\Delta v_{transfer} + \Delta v_{HOI} = 76.59 \text{ m/s}$. From this value the mass of the satellite at the beginning of the science phase can be retrieved as $m_{0,science} = 1785.5 \text{ kg}$, which, along with $m_{prop,SRP}$, can be used in the Tsiolkovsky's equation to estimate the total cost of the desaturation manoeuvres:

$$\Delta v_{att,est} = I_{sp} g_0 \ln \left(\frac{m_{0,science}}{m_{0,science} - m_{prop,SRP}} \right) = 11.48 \text{ m/s} \quad (43)$$

This value is way lower with respect to the value of 43 m/s, which means that there is a large margin to allow several slew manoeuvres in case of emergencies.

5 Thermal Control Subsystem

5.1 Introduction

The Thermal Control Subsystem (TCS) shall guarantee the following major requirements:

- Maintain all equipment mounted on the PLM structure within acceptable temperature range limits
- Provide a stable thermal environment in order to meet all the pointing requirements of the AOCS and experiment sensors
- Provide an acceptable radiative environment for the experiment sensors

The thermal design is based on passive means (MLIs, paints, washers, doublers, etc.) and on heater lines, controlled by devoted thermistors.

The thermal environment of SOHO is particularly stable, mainly because of the absence of eclipses since it is a solar observer situated at L1. In the nominal environment, the spacecraft is constantly facing the Sun exposing always the same surfaces to the only significant heat source.

Nevertheless, the design shall consider some particular conditions [26]:

- During the Early Operational phase, with respect to the nominal condition, the S/C configuration is totally different from the thermal point of view;
- To be compliant with Failure Case, the thermal design must be compatible with very different environmental conditions

5.2 Basic Configuration

The thermal design has two basic configurations regarding environmental constraints:

- **Halo Orbit:** the S/C is $+X_B$ oriented with solar arrays open. The satellite is in L1, meaning that no external heat input other than direct solar flux has to be taken into account.
SVM's radiators are perpendicular to the Sun Direction and only solar reflection from the solar arrays goes to the $\pm Y_B$ oriented panels. The upper platform will be partially shadowed by the PLM and the lower one, as well as the Antenna Pointing Assembly, will be totally in shadow, continuously looking to deep space.
- **Early Operational Phase:** Composed by three main subphases: Parking, Insertion and Initial Sun Acquisition (ISA).

The SVM has important differences with the nominal configuration foreseen in for Halo:

- Solar arrays initially stowed: $\pm Y_B$ panels radiator do not have any view factor towards space
- Centaur and SOHO are attached (Parking and Insertion subphases)
- Power dissipation of units are different
- External S/C environment is different (e.g. Earth input)

5.3 Architecture

The S/C thermal design is highly influenced by the Sun's pointing requirement and relies on classical thermal control hardware. The SVM is thermally controlled by wrapping its structure with an MLI blanket, leaving the radiators uncovered [26]. The upper enclosure of the PLM is covered by a sun shield that acts as a radiator for instruments and the electronics placed on the $+X_B$ panel. On the rear side of the OSR, some adjustable heaters were installed to account for the ageing of the material

and for changes in the solar cycle. Different paints are used inside and outside to achieve temperature homogeneity.

The PLM provides the instruments with the smallest possible thermo-elastic distortion and the adequate thermal environment. To this aim, the instrument sensors are mounted on the 4 upper lateral panels ($\pm Z_B$ and $\pm Y_B$) and the $+X_B$ panel, under the sunshield, together with few S/S units. Those panels are covered with MLI blankets too. When non-operational, each sensor is temperature controlled by S/C powered "substitution" heaters, through duty cycle adjustments.

Moreover, for SOHO-SVM, there are extra requirements that eventually give the approach to the MLI basic design:

- No contamination of PLM experiments (venting to $-X_B$ axis direction, and no fibreglass spacer)
- Minimum heat interchange with the PLM, including reflection of external sheets of MLIs because of the low operative temperature required by the scientific instruments
- External surfaces should be electrically conductive to avoid the build-up of different electric potentials on the surfaces since the s/c is directly exposed to the solar wind during all its operative lifetime
- Thermal stability of PLM-SVM interface, short and long term

All experiment sensor units (except for VIRGO) perform their own thermal control; the PLM thermal control thus only guarantees the temperature range of their temperature reference points and their radiative environment, through the definition of appropriate heat sink temperatures. For the other units (i.e. VIRGO and all electronic units except MDI and LASCO electronics), the PLM is in charge of the full thermal control.

The PLM thermal control also provides the lines for the substitution heaters which are activated when their associated experiment units are not powered. The basic concept of the PLM thermal control is to use a heater fixed power mode with adjustable power levels for each heater circuit, which is commandable from the ground.

5.4 Single-Node Analysis

5.4.1 Assumptions and properties

In this section, a preliminary thermal analysis using one node in steady-state conditions is presented. First of all, being the volume of the spacecraft $V = 42.38 \text{ m}^3$, an equivalent sphere model is adopted, in order to retrieve an equivalent cross-section area for the incoming solar power computation and an equivalent surface area for the IR and albedo powers computation, that resulted in $A_{eq,sph} = 58.78 \text{ m}^2$, $A_{cross} = 14.70 \text{ m}^2$.

The thermo-optical properties considered for the S/C are summarized in the table below, along the constants used for the computations:

$\dot{q}_0 [\frac{W}{m^2}]$	$a [-]$	$\theta [\text{rad}]$	$T_{DS} [\text{K}]$	$\alpha_{low} [-]$	$\alpha_{high} [-]$	$\epsilon [-]$	$\epsilon_{rad} [-]$
1367.5	0.35	0	0	0.14	0.92	0.78	0.96

Table 18: Constants and thermo-optical properties

It is important to highlight that for the incoming solar flux, an equivalent absorptivity is considered. In fact, the surface facing the Sun is modelled as a composition of low (only the Sun shield) and high absorbing surfaces, considering also the panels. Weighting α_{low} and α_{high} on the corresponding fraction of occupied surface, α_{eq} is computed as:

$$\alpha_{eq} = \frac{\alpha_{low} 1.4^2 + \alpha_{high} (3.65 \cdot 9.5 - 1.4^2)}{3.65 \cdot 9.5} = 0.88 \quad (44)$$

On the other hand, only α_{high} is considered for the surface facing the Earth, which is assumed to be completely illuminated by the Sun.

Furthermore:

- The S/C has the same configuration in both the phases
- The Sun and the Deep Space are black bodies
- The Earth is considered at $T_{Earth} = 250 K$ and with $\epsilon_{Earth} = 0.8$.
- Only radiation has been considered
- In the Hot case, all the Earth portion seen from the S/C is illuminated
- The internal power is computed considering that all devices and subsystems dissipate entirely the input power into thermal energy, overestimating this contribution in both cases (hot and cold).

5.4.2 Hot and cold case selection

The analysis is performed differentiating between the hot and the cold worst cases. Since the transfer trajectory covers only 1% of the distance from the Earth to the Sun, the variation of solar flux along the whole transfer arc results low (about 2%). In fact, the main heat flux change is due to the presence/absence of the albedo and IR radiation from Earth.

Consequently, the hot case takes place during the first part of the transfer trajectory. However, right after the detachment from the Centaur upper stage, SOHO experiences a thermal transient which does not allow to adopt steady-state assumption. This transient can be considered extinguished after the ISA phase, which lasts about 2 hours from the upper stage detachment and, from ephemeris, corresponds to an altitude of approximately 30000 km.

On the other hand, the coldest case takes place under conditions where the contribution of Earth's radiation can be deemed negligible and the distance from the Sun is not at its minimum. Nonetheless, due to the highly similar circumstances at the Lagrange point, and given its greater significance for the satellite's thermal design, along with the stationary nature of the case, this latter condition has been prioritized for thermal analysis.

For the two cases, data on the internally generated power have been retrieved from literature [27]. Its maximum value associated with the hot case is $\dot{Q}_{int,max} = 933 W$, while the minimum value associated with the cold case is $\dot{Q}_{int,min} = 454 W$, with all the instruments turned off.

5.4.3 Hot Case

Firstly, it is necessary to define the total incoming heat power during the ISA phase starting from detachment ($\approx 1320 km$ of altitude from ephemeris) to the end of this phase ($30000 km$ of altitude). This value, for each distance, is computed as the sum of the heat powers as follows⁶:

$$\dot{q}_{Sun-S/C} = \dot{q}_0 \left(\frac{R_{Sun-Earth}}{R_{Sun-S/C}} \right)^2 \quad (45)$$

$$\dot{q}_{albedo} = \dot{q}_{Sun-S/C} a \cos\theta \left(\frac{R_{Earth}}{R_{Earth-S/C}} \right)^2 \quad (46)$$

$$\dot{q}_{IR} = \sigma_0 \epsilon_{Earth} T_{Earth}^4 \left(\frac{R_{Earth}}{R_{Earth-S/C}} \right)^2 \quad (47)$$

$$\dot{Q}_{tot} = \dot{Q}_{Sun} + \dot{Q}_{albedo} + \dot{Q}_{IR} = A_{cross} \alpha_{eq} \dot{q}_{Sun-S/C} + A_{eq,sph} \alpha_{high} \dot{q}_{albedo} + A_{eq,sph} \alpha_{high} \dot{q}_{IR} \quad (48)$$

Using a proper discretization of the distances, the mean value of all the corresponding total heat powers is considered as the equivalent total heat power useful to carry out the steady-state analysis and it is

⁶The formulas adopted to evaluate the specific heat fluxes are reported in the appendix

$\dot{Q}_{mean} = 22985.52 W$, which corresponds to an equivalent steady-state altitude of $9999.26 km$. In fact, using Equations 45 to 48 for this altitude value, the equivalence is given by the same total incoming heat power:

$$\dot{Q}_{tot} = \dot{Q}_{Sun} + \dot{Q}_{albedo} + \dot{Q}_{IR} = (17605.83 + 3926.44 + 1453.25)W = 22985.52 W = \dot{Q}_{mean} \quad (49)$$

From the power balance, the total heat power received from these three sources is emitted towards the deep space as:

$$\dot{Q}_{DS} = \sigma_0 \epsilon A_{eq,sph} (T_{s/c}^4 - T_{DS}^4) \quad (50)$$

Consequently, the temperature of the spacecraft as a single node can be computed as:

$$T_{S/C} = \left(\frac{\dot{Q}_{int,max} + \dot{Q}_{tot}}{\sigma_0 \epsilon A_{eq,sph}} + T_{DS}^4 \right)^{\frac{1}{4}} = 309.71 K \quad (51)$$

Considering that the constraint on the maximum temperature is dictated by the batteries, which cannot exceed $40^\circ C$, and adopting an uncertainty margin of $\pm 15 K$, in the worst case $T_{max} = 313.15 - 15 = 298.15 K$. The resulting temperature of the spacecraft exceeds this maximum allowed value, so it is necessary to size the required minimum area of radiators in order to dissipate more heat, assuming an emissivity of $\epsilon_{rad} = 0.96$:

$$A_{rad,min} = \frac{\dot{Q}_{int,max} + \dot{Q}_{tot}}{\sigma_0 \epsilon_{rad} (T_{max}^4 - T_{DS}^4)} - \frac{\epsilon}{\epsilon_{rad}} A_{cross} = 7.85 m^2 \quad (52)$$

Beneath the assumptions adopted for the single-node analysis, these radiators are assumed to be placed as appendages the aim of which is just to emit towards the deep space without participating in the absorption of the fluxes.

5.4.4 Cold Case

The cold case occurs during the science phase around the L1 point which is already a steady-state condition, so the new distances are approximated as $R_{Sun-s/c} = 0.99 AU$ and $R_{Earth,s/c} = 0.01 AU$. This, adopting the equations 45 to 48, leads to new incoming powers and in particular the solar one $\dot{Q}_{Sun} = 17959.36 W$ is now several orders of magnitude greater than the albedo and IR powers, which are respectively $\dot{Q}_{albedo} = 0.48 W$ and $\dot{Q}_{IR} = 0.17 W$. These results prove that the cold case has been well associated with the halo orbit, and the last two powers are negligible for this analysis. Consequently, the resulting temperature of the spacecraft is:

$$T_{S/C} = \left(\frac{\dot{Q}_{int,min} + \dot{Q}_{Sun}}{\sigma_0 \epsilon A_{eq,sph}} + T_{DS}^4 \right)^{\frac{1}{4}} = 290.11 K \quad (53)$$

Considering that the hydrazine freezing point is $275.15 K$, the minimum temperature with the same uncertainty margin of the hot case is $T_{min} = 275.15 + 15 = 290.15 K$. It is evident that heaters are required to warm up the spacecraft and to maintain its temperature within the range. In order to do that, the amount of minimum power needed is:

$$\dot{Q}_{heaters} = \sigma_0 \epsilon A_{eq,sph} T_{min}^4 - \dot{Q}_{int,min} - \dot{Q}_{Sun} = 11.41 W \quad (54)$$

5.5 Multi-Nodal Analysis

5.5.1 Model definition

In order to refine the results from the single-node analysis, a simple multi-nodal analysis has been carried out, including three thermal nodes in correspondence of the PLM, SVM and solar panels (SP).

Despite the case studies being the same as the single-node analysis, the emissivity of the S/C has been considered to be different from the previous case and equals $\epsilon = 0.35$. This modification is supported by the fact that, with respect to the single-node approach, in this case the total surface area is far larger than the one of the equivalent sphere, leading to an increase of the emitted power.

Furthermore, considering $\epsilon_{rad} = 0.96$ it is reasonable to assume a lower value for the rest of the S/C, which is achievable through a dedicated MLI.

For each node, a different temperature range has been considered:

- $T_{PLM} \in 243 \div 303 K$, where the main constraint is the operative range of the Star Sensor
- $T_{SVM} \in 253 \div 303 K$, where the main constraint is the operative range of the batteries
- $T_{SP} \in 123 \div 423 K$, considering a typical operational range

Additionally, to the assumption made for the single node case, other assumptions are made:

- In the cold case the contribution from the Earth (IR + Albedo) can be neglected
- The S/C has the same configuration in both of the phases (SP open)
- The SVM has no radiation contribution from the Sun (both cases)
- The PLM has no radiation contribution from the Earth (hot case)
- Only radiative thermal exchange has been considered

5.5.2 Sizing

The thermal equilibrium condition at every node leads to the following system of equations:

$$\begin{cases} \dot{Q}_{PLM,DS} = \dot{Q}_{Sun,PLM} + \dot{Q}_{SP,PLM} \\ \dot{Q}_{SVM,DS} = \dot{Q}_{SP,SVM} + \dot{Q}_{Alb,SVM} + \dot{Q}_{IR,SVM} \\ \dot{Q}_{SP,PLM} + \dot{Q}_{SP,SVM} + \dot{Q}_{SP,DS} = \dot{Q}_{Alb,SP} + \dot{Q}_{IR,SP} + \dot{Q}_{Sun,SP} \end{cases} \quad (55)$$

where every couple of subscripts indicate, respectively, the heat source and the heat sink. The dependency from the nodes' temperatures is made explicit as follows:

$$\dot{Q}_{SP,PLM} = \frac{2\sigma_0 (T_{PLM}^4 - T_{SP}^4)}{\frac{1-\epsilon_{SP}}{\epsilon_{SP} A_{SP}} + \frac{1}{A_{SP} F_{SP \rightarrow PLM}} + \frac{1-\epsilon_{PLM}}{\epsilon_{PLM} A_{PLM}}} \quad (56)$$

$$\dot{Q}_{SP,SVM} = \frac{2\sigma_0 (T_{SVM}^4 - T_{SP}^4)}{\frac{1-\epsilon_{SP}}{\epsilon_{SP} A_{SP}} + \frac{1}{A_{SP} F_{SP \rightarrow SVM}} + \frac{1-\epsilon_{SVM}}{\epsilon_{SVM} A_{SVM}}} \quad (57)$$

$$\dot{Q}_{PLM,DS} = 2\sigma_0 \epsilon_{PLM} T_{PLM}^4 A_{PLM} F_{PLM \rightarrow DS} \quad (58)$$

Equation 58 equally holds for the SVM and SP, considering the respective areas and view factors for each surface facing the deep space.

$F_{S/C \rightarrow Sun}$	$F_{S/C \rightarrow Earth}$	$F_{SP \rightarrow SVM}$	$F_{SP \rightarrow PLM}$	$F_{SVM \rightarrow SP}$	$F_{SVM \rightarrow DS}$	$F_{PLM \rightarrow SP}$	$F_{PLM \rightarrow DS, side}$	$F_{PLM \rightarrow DS, top}$	$F_{SP \rightarrow DS, top}$	$F_{SP \rightarrow DS, down}$
$2 \cdot 10^{-5}$	0.1517 or 0^7	0.0400	0.0700	0.0850	0.9150	0.2298	0.7702	0.99998	0.8900	0.8483

Table 19: View factors

Which leads to the following nodes' temperatures:

	<i>Hot case</i>	<i>Cold case</i>
T_{PLM}	304.42 K	282.98 K
T_{SVM}	289.07 K	256.23 K
T_{SP}	436.46 K	420.34 K

Table 20: Nodes' temperatures

⁷0 is the value for the Cold Case

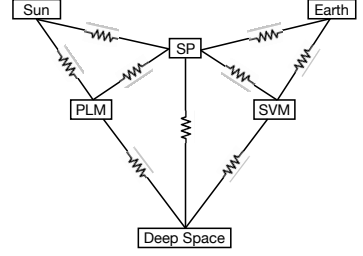


Figure 12: Electrical Scheme

To comply with the requirements of the operative range, considering a temperature margin of $\pm 15 K$, radiators are needed both for the PLM and the SVM in the hot case and heaters are needed for the SVM in the cold case.

Considering a radiator emissivity of $\epsilon_{rad} = 0.96$, the resulting area that must be covered by radiators is $A_{rad,PLM} = 1.66 m^2$ and $A_{rad,SVM} = 0.1 m^2$ which provide the S/C with additional dissipated powers of respectively 620.84 W and 38.75 W.

On the other hand, the resulting needed power for the heaters is $Q_{heaters} = 362 W$.

5.6 System Budgets

5.6.1 Mass Budget

Considering $6 kg/m^2$ as areal density for the radiators, the total mass results in $m_{rad} = 10.57 kg$, considering the results obtained in the multi-nodal approach.

MLIs, heaters and thermocouples' masses are considered negligible.

5.6.2 Data Budget

For what concerns the data budget, only the thermocouples have been considered, assuming the following considerations for their positioning:

- 2 per payload (24 total), both for redundancy and to check the temperature gradient and maintain the payloads in their operative ranges
- 4 per side of each panel (48 total), in order to check that the radiated power corresponds to the nominal one and that there are no unexpected rotations
- 4 per solar panel (8 total);
- ≥ 15 for the electronic components of the SVM and PLM (processors, batteries, memories etc.).

Considering that each measurement is allocated on the onboard computer as a *16 bit* number and that a sampling frequency of $0.001 Hz$ is used to avoid an excessive amount of data, the overall data rate results in $1.9 Bps$.

5.6.3 Power Budget

The resulting power needed by the heaters ($362.32 W$) is more than dedicated to the TCS of the SVM cited in [27], which is $133 W$.

Clearly, the aforementioned result is too high, meaning that a more refined analysis should be conducted, by introducing internal heat exchange and increasing the number of nodes.

It is important to notice that on the actual S/C, heaters and radiators are used locally to intervene on specific components that require different temperatures from the average one and for this reason are designed along with the single TCSs of the different items.

6 Electric Power Subsystem

6.1 Introduction

The Electrical Power Subsystem (EPS) of the Solar and Heliospheric Observatory plays a pivotal role in the operation of the spacecraft. The EPS is responsible for generating, storing, and distributing electrical power to all of SOHO's scientific instruments, onboard computers and communication systems.

The primary requirements for the EPS include high reliability, to ensure continuous power during the mission, sufficient capacity, to handle peak power demands, and robust safeguards to protect against power surges and other anomalies.

6.2 Architecture

The entire Electric Power Subsystem is placed in SOHO's SVM. The power subsystem provides regulation, protection and distribution of $\approx 1400\text{ W}$ (EOL) of solar-array power, supported by two 20 Ah Nickel-Cadmium batteries of 32 cells each. The main spacecraft power bus is regulated to $28\text{ V} \pm 1\%$ with a three-domain regulation of solar-array shunt mode, battery discharge and battery charge mode. The batteries are sized to deliver power during the Initial Sun Acquisition phase and for peak power request (950 Wh).

All power lines to users are protected by latching-current limiters.

All electrical power subsystem functions are redundant, including connector redundancy all the way from the solar array and battery inputs to the power distribution outputs.

The solar arrays consist of 2 wings ($\pm Y$ direction), each consisting of 2 solar panels and 1 yoke panel. The solar cells are $2\text{ }\Omega\text{cm}$ BSR silicon solar cells and the cover glass is a CMX-type. Cell interconnections are made of a $20\text{ }\mu\text{m}$ thick silver sheet with stress relief loops in the series direction.

6.2.1 Architecture rationale

Thanks to a permanent Sun-pointing attitude and since no eclipse occurs during its lifetime, nominally, no secondary source would be requested since the solar panels are positioned to be always exposed to solar radiation in normal mode. However, two batteries have been designed for ISA mode, ESR mode (in which Sun-pointing is not assured) and to fulfil peak power demand.

In particular, the Nickel-Cadmium combination has been selected for the batteries due to its inherent high energy density, long cycle life, wide operating temperature range, fast charging capability, and reliable performance. Furthermore, lithium-ion batteries had not yet been tested enough for being mounted on a spacecraft at that time.

The primary function of a latching-current limiter (LCL) is to protect the electrical system from overcurrent conditions. By limiting the current flow to a safe level, LCLs prevent damage to sensitive electronics and wiring.

No RTG has been used due to the ESA's policies about nuclear devices on board and the absence of eclipses.

6.3 Sizing

In order to establish the most crucial electrical power request during the mission, a preliminary analysis of the power budget per each subsystem has been carried out. The results are reported hereafter, having taken into account the modes considered to be the most power-demanding:

S/S	Normal Mode	Manoeuvre (SK-MM)	ESR
PS	0 W	28 W	0 W
TTMTC + OBDH	117.6 W	117.6 W	120.40 W
TCS	303 W	303 W	303 W
P/L	625 W	0 W	0 W
AOCS	94.7 W	164.70 W	47.60 W
EPS	28 W	28 W	28 W
Total	1168.30 W	613.33 W	499 W
Total Margined (+20%)	1401.96 W	735.99 W	598.80 W

Table 21: Power Budget

From Table 21 it is clear that the primary energy source has to be sized with respect to the Normal Mode since it is the one during which all the subsystems have to guarantee the optimal conditions for the scientific instruments to work properly.

6.3.1 Solar Array

The power bus is maintained at an approximately constant voltage ($28 \pm 1\%$) [28] by a DET (Direct Energy Transfer) control on the energy source. This strategy consists of a dissipative control, acting on the current, through shunt regulators.

The choice of a DET control system is due to its inherent higher efficiency factor X_d with respect to the alternative PPT (Peak Power Transfer) control one, as well as the simpler and lighter architecture. However, a PPT would guarantee a more accurate control, since, acting on the voltage, the bus would always operate at its optimum condition, preserving the health of the batteries more. On the other hand, the PPT strategy would have been more suitable if the mission was facing a high number of cycles related to eclipse scenarios, opposite to the constant sunlight exposure condition of SOHO in L1⁸.

Considering the aforementioned considerations, the following data can be exploited during the sizing of the primary energy source, which are the solar panels. In particular, the solar flux has been considered as if the S/C is at the Earth's distance from the Sun, in order to be conservative, considering the minimum value for this variable along the whole mission.

Daylight Data	
X_d	0.85
P_d	1401.96 W
p_0	$1367 \frac{W}{m^2}$

Table 22: SA sizing data

From Table 22 the actual power requested to the solar arrays can be computed:

$$P_{SA} = \frac{P_d}{X_d} = 1649.36 W \quad (59)$$

For what concerns the solar cells, the following parameters have been considered [29]:

⁸The yearly fluctuation in Sun intensity is $\approx 6\%$ between the winter solstice (warmer) and the summer one (colder).

Solar Cells	
ε_{BOL}	0.132
dpy	0.02
p	$25 \frac{W}{m^2}$
I_d	0.77
U_{cell}	0.404 V
A_{cell}	$0.0024 m^2$

Table 23: Solar Cells data

where ε_{BOL} is the efficiency of the cell [23], dpy is the degradation per year, p is the specific power and I_d is the inherent degradation⁹.

The specific power input to the SA can be computed as:

$$p_{in} = \varepsilon_{BOL} p_0 = 180.44 \frac{W}{m^2} \quad (60)$$

Given that the average inclination between the array surface normal and the Sun direction is taken as $\theta = 25^\circ$, the actual specific power produced by the SA at BOL reads:

$$p_{BOL} = p_{in} I_d \cos(\theta) = 125.92 \frac{W}{m^2} \quad (61)$$

Considering the panels' dpy and the lifetime of the S/C (6 years), it is possible to compute the lifetime degradation and the corresponding specific power at EOL:

$$L_{life} = (1 - dpy)^{T_{life}} = 0.8858 \quad (62)$$

$$p_{EOL} = L_{life} p_{BOL} = 111.55 \frac{W}{m^2} \quad (63)$$

From the requested output at EOL and given the array's layers composition [29] [30], it is possible to compute its area¹⁰ and mass¹¹:

$$A_{SA} = 0.9 \frac{P_{SA}}{p_{EOL}} = 13.31 m^2 \quad (64)$$

Component	Density $\left[\frac{Kg}{m^3}\right]$	Thickness [mm]
Cover Glass (CMX)	2600	0.1
Si	2330	0.21
Al_{honey}	123	22

Table 24: SA layers data

$$m_{SA} = A_{SA} (\rho_{Si} t_{Si} + \rho_{CMX} t_{CMX} + \rho_{Al,honey} t_{Al,honey}) = 45.98 kg \quad (65)$$

In order to refine the results, the single solar cell voltage and the single solar cell surface, reported in Table 23, have been considered, along with the overall system voltage $U_{sys} = 28 V$.

⁹For what regards the specific power p and the inherent degradation I_d , typical values for Si cells have been assumed.

¹⁰A 10% margin has been considered on the surface of the SA, in order to account for connections between cells.

¹¹The computation includes only the aluminium honeycomb, the solar cell and the protection glass.

Given the total surface datum, it is possible to compute the number of cells needed to cover the surface of the entire array:

$$N = \left\lceil \frac{A_{SA}}{A_{cell}} \right\rceil = 5518 \quad (66)$$

Moreover, from the voltage information, the number of cells placed in series can be obtained as follows:

$$N_{series} = \left\lceil \frac{U_{sys}}{U_{cell}} \right\rceil = 70 \quad (67)$$

Because of the necessary integer roundings applied in the previous computations, some corrections are needed.

Concerning the actual system voltage, it becomes:

$$U_{real} = N_{series} U_{cell} = 28.28 V \quad (68)$$

Accordingly, the number of cells needed to grant the desired power reads:

$$N_{real} = \left\lceil \frac{N}{N_{series}} \right\rceil N_{series} = 5530 \quad (69)$$

Eventually, the real total area of the SA is:

$$A_{SA,real} = N_{real} A_{cell} = 13.34 m^2 \quad (70)$$

In order to compare the obtained results with the real ones, the disposition of the solar panels is reported below:

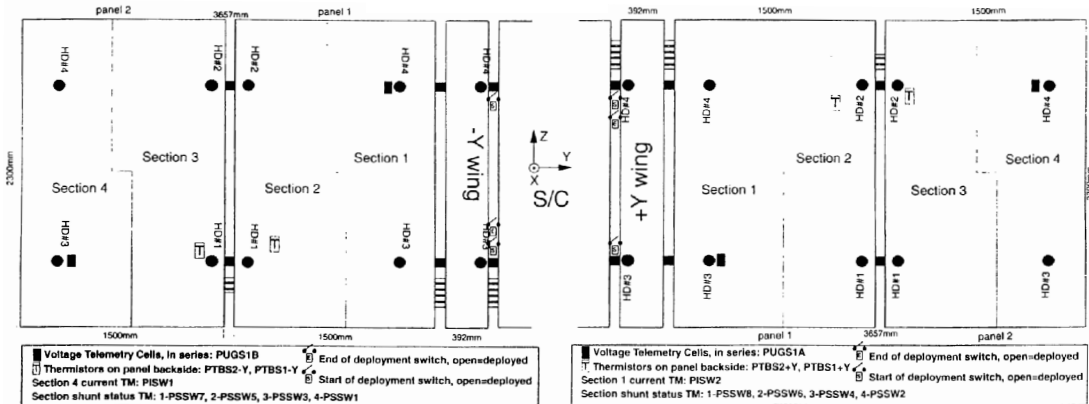


Figure 13: SA actual configuration

The main difference lies in the total surface area and number of cells values. The first one, computed in Equation 70 and slightly different from the actual $13.8 m^2$ value. The second one, on the other hand, available from Equation 66, presents a more significant difference from the real value, 4944 [29].

These differences are for sure linked one to each other and mainly due to the inexact 10% margin considered for the interconnections, as well as the assumed values for the computation of p_{EOL} .

6.3.2 Batteries

The secondary energy source are two NiCd batteries, put in parallel in order to increase the overall available capacity.

In Table 25 the specific data for this type of battery, used for the sizing are reported. In particular $U_{sys,batt}$, P_{peak} and η values have been respectively taken from [28], [15] and [31]. Regarding the remaining values, typical data have been assumed.

Battery Data	
Type	NiCd
$U_{sys,batt}$	45 V
C	900 Wh @ 45 V
P_{peak}	950 Wh
E_m	40 $\frac{Wh}{kg}$
E_v	90 $\frac{Wh}{dm^3}$
η	0.7
$U_{cell,batt}$	1.35 V
DOD	0.9

Table 25: Single Battery data

Firstly, from the single battery capacity and the peak power request it is possible to compute the number of batteries needed to grant the requested power:

$$N_{batteries} = \left\lceil \frac{C}{(DOD)\eta P_{peak}} \right\rceil = 2 \quad (71)$$

Accordingly, the mass and volume of the batteries read:

$$m_{batt} = \frac{C}{E_m} = 22.5 kg \quad (72)$$

$$V_{batt} = \frac{C}{E_v} = 10 dm^3 \quad (73)$$

Once more, in order to refine the results, it is possible to determine the number of needed cells to put in series to obtained the desired voltage, starting from the voltage of the battery and the voltage of a single cell. A single battery is considered in the following computations.

$$N_{series} = \left\lceil \frac{U_{sys,batt}}{U_{cell,batt}} \right\rceil = 34 \quad (74)$$

The corresponding actual voltage obtained in a cell series is:

$$U_{real} = N_{series} U_{cell} = 45.9 V \quad (75)$$

Therefore, the capacity of a single string is:

$$C_{string} = \mu C_{cell} U_{real} = 734.4 Wh \quad (76)$$

where a package efficiency $\mu = 0.8$ has been considered.

Eventually, the number of cell strings to put in parallel in order to obtain the desired 950 Wh and the respective battery capacity are computed as follows:

$$N_{parallel} = \left\lceil \frac{C}{C_{string}} \right\rceil = 2 \quad (77)$$

$$C_{real} = N_{parallel} C_{string} = 1468.8 \text{ Wh} \quad (78)$$

Comparing the obtained results for the batteries with the real configuration, the values are very similar to the actual ones. The main differences can be found in the number of cells to put in series in the latter single-battery approach and in the total battery capacity.

The obtained value for the first one is 34, while every battery contains 32 cells put in series [29]. On the other hand, the second value presents a larger discrepancy, being 1468.8 Wh instead of 1800 Wh . Both these differences, as well as the ones encountered in the SA sizing, are due to the previous assumptions on some values, in particular $U_{cell,batt}$, η , DOD and μ .

6.4 Budgets

6.4.1 Data Budget

The data acquisition is characterized by a 15 s sampling period (0.07 Hz) and down-linked to the NASA DSN ground stations and routed to the NASA GSFC. Except for specific purposes of min-max searches, the daily averages of the last day of the month are used for the long-term performance evaluation. All analogue measurements are converted into 8-bit TM parameters. [28]

Mnemonic	Type	Description	LSB
PISW1	I_{sc}	Short circuit current, solar array section 1	40mA
PISW2	I_{wp}	Working point current, solar array section 8	40mA
PUGS1A/B	V_{oc}	Open circuit voltage	20mV
PTGS1+/-Y	T_{ob}	Temperature back side inner panels	2.2°C
PTGS2+/-Y	T_{sh}	Temperature back side outer panels	2.2°C
PSSW1-8	bi-level	Status of shunt sections: shunting or on-bus	
PIMB1/2	I_{load}	Mainbus current	230mA
PUBATVT1	V_{bat1}	Voltage Battery1	207mV
PUBATVT2	V_{bat2}	Voltage Battery2	207mV
PTBAT1A/B	T_{bat}	Temperature Battery1	0.27°C
PTBAT2A/B	T_{bat}	Temperature Battery2	0.27°C

Figure 14: EPS Telemetry parameters

Considering the measurements listed in Figure 14, each year 23.12 MB are produced.

6.4.2 Mass and Volume Budget

The total mass and volume of the Electrical Power Subsystem can be computed as the sum of the solar array and the batteries.

$$m_{EPS} = 1.2 (m_{SA} + m_{batteries}) = 82.18 \text{ kg} \quad (79)$$

$$V_{EPS} = 1.2 (V_{SA} + V_{batteries}) = 307.62 \text{ dm}^3 \quad (80)$$

A typical 20% margin has been considered for the mass value, in order to take into account the cabling and harness' presence. The same margin has been assumed to be reasonable also for the volume computation.

7 Configuration

7.1 General considerations

The SOHO spacecraft overall configuration has been dictated by the major requirement of providing easy mounting and accessibility to the P/L instruments while satisfying all their functional requirements. Due to the nature of the mission, particular attention has been given to their viewing direction, FOV clearance, stray-light avoidance and pointing stability, along with other specific requirements.

The satellite are conceptually and physically divided in two main elements, linked by a simple bolted circular interface, according to a modular concept:

- **Payload Module (PLM):** It contains all the scientific instruments and some of the attitude sensors.
- **Service Module (SVM):** It is where all the housekeeping equipment is located, and it can be further divided into two sub-assemblies:
 - service equipment module;
 - propulsion module.

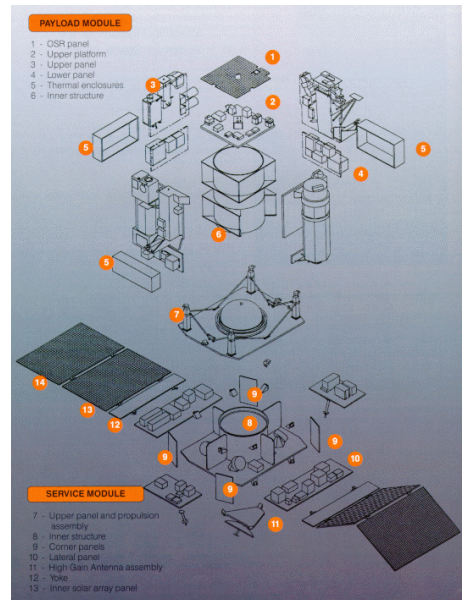


Figure 15: General configuration

An elongated configuration has been selected, in order for the S/C to properly fit inside the launcher's payload bay, as well as to reduce the cross section that faces the Sun, thus reducing the dimension of the sun-shield. Furthermore, with this configuration the main electronics of the SVM are screened by the PLM from Sun-emitted particles and the P/L instruments are less exposed to the electromagnetic interference produced by the SVM, being relatively far from them. The entire set of equipment has been positioned with the aim of minimising the distance between the center of mass and the geometrical center of the S/C, in particular along the X_B Sun-pointing axis.

7.1.1 Folded configuration

The spacecraft is launched in a folded-panels configuration, in order to reduce the occupied volume inside the launcher's payload bay and to limit the vibrations transferred both by the launcher itself, through the adaptor, and by the acoustic loads generated during the ascent, to all the free appendages. It is important to notice that even in this folded configuration, the solar panels do not cover the thrusters, sensors and payloads, which are used in the first phases of the mission, when the S/C is powered by the batteries. The SA is deployed only after the detachment with the Centaur upper stage. During launch, the LGAs are folded and the HGA is rigidly attached to the spacecraft and they are both released only after spacecraft separation.

An image of the tilted configuration is reported in Appendix C.

7.2 Payload Module

The PLM consists of four upper panels, to support experiment sensors at their outside and three lower panels support experiment electronics. A central tube provides load transfer to the SVM central tube via the propulsion support ring. The Sun shield on top is connected to the PLM through small arms made of an insulator material, in order to avoid any thermal conduction.

7.2.1 Scientific instruments

The Scientific instruments are disposed mainly around the Sun shield for the following reasons:

- maximize the FOV;

- most of them are too big to be inserted inside the PLM panels;
- the Sun shield would have to be perforated in order to let the sensors see the Sun, reducing the shielding properties.
- leave the space inside the panels for some of the electronics.
- enable thermal decoupling from the S/C, in order to let the different instruments work at their different operational temperatures.

Accordingly with the last point, all experiment sensor units (except for VIRGO) perform their own thermal control. Since VIRGO is the smallest one among all the instruments and could be placed inside the PLM, it is placed behind the Sun shield, allowing its FOV to cover the Sun through a hole. The arrangement of the instruments around the shield has been studied to ensure that the center of mass is aligned with the X_B axis. Another consideration can be made for SWAN [32], which does not require a strict Sun-pointing. This reason, together with the general aim of optimizing space allocation, led to its lower positioning with respect to the rest of the instruments. With a view to the pointing accuracy, in general, the scientific instruments are connected to the main structure.

7.2.2 PLM Sensors and Electronics

Most of the attitude control sensors are accommodated onto the PLM, in order to benefit from its high stability with regard to experiments (FPSS, SSU), or to have a direct view to the Sun direction (Solar Acquisition Sensor (SAS)). The latters are arranged in a configuration giving omni-directional coverage, in order to work even in ESR mode, recovering the Sun acquisition and, subsequently, the nominal attitude. The FPSSs are placed on the side of the Sun shield, while the star sensors are positioned along the $+Z_B$ axis, to avoid them pointing directly towards the Sun. Furthermore, with this positioning, they receive less reflected light from the solar panels. Both the FPSSs and the star trackers are arranged in a doublet configuration, in order to grant redundancy.

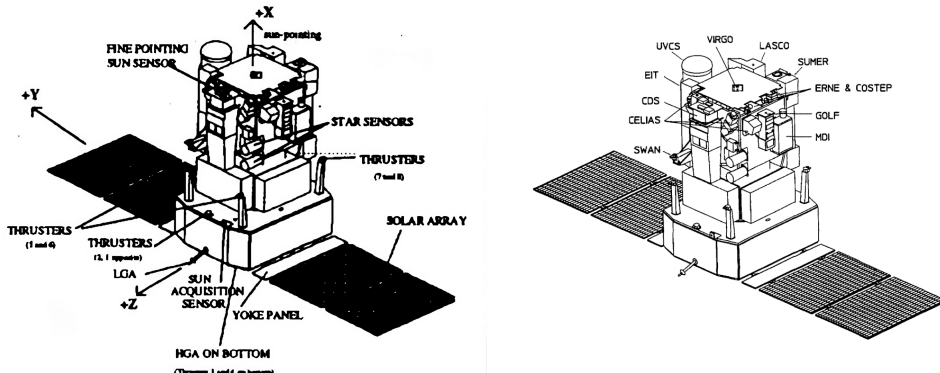


Figure 16: PLM sensors and scientific instruments disposition

7.3 Service Module

The SVM is a box-shaped structure made of aluminium honeycomb panels attached to a corrugated aluminium cylinder by four shear webs.

The box's upper floor houses the propulsion subsystem, tank and thruster masts. The SVM includes the following subsystems: ANTS (Antenna Subsystem), COBS (Central On-Board Software), AOCS, PS, EPS, SGS (Solar Generator Subsystem), TCS and SHS (Structure and Harness Subsystem).

As it is clearly shown in Figure 18, each subsystem is located on a dedicated panel and near its respective interface units (PDU, RTU). In order to simplify as far as possible the data interfaces, the TM & TC functions are combined in three RTUs, which operate under the control of the main computer via the OBDH bus. The aforementioned RTUs are dedicated, respectively, to the PLM, the SVM equipment, and the Attitude Control Unit (ACU). The system is fully redundant. Moreover, an independent hardwired mode provides a safe mode in failure cases [15].

7.3.1 Propulsion subsystem

As aforementioned, the modular requirements of the S/C have been respected also for the propulsion module, allowing an easy implementation. The main feature of the configuration is the fact that none of the thrusters generates a plume that impacts neither the S/C body nor the SA. None of the generated Δv point, indeed, neither towards the S/C main body nor the $\pm Y_B$ direction.

Thrusters 1 and 2, which generate a Δv in the $-X_B$ direction, are mounted with an angle outwards in order to not impinge the P/L instruments, respecting their cleanliness requirements.

Thrusters 3 and 4, are mounted on the bottom surface of the SVM, in order not to impinge the solar panels, thus compromising their operability.

Thrusters From 5 to 8 are placed at the same height of the center of mass, in order to avoid unsolicited torque during their firing.

Furthermore, in this configuration all the 3 axes control is permitted by the actuators even in case of failures of some of them.

For what concerns the tank, it is displaced in the middle of the module to reduce the length of the feeding lines (thus the respective pressure drops) and to limit the variation of the center of mass only along the Z_B direction during the fires.

7.3.2 Service Equipment Module

This module houses the rest of the subsystems together with the solar panels, that are rigidly mounted along the $\pm Y_B$ axis on the SVM lower end, not to interfere with the P/L. Since they are always exposed to the Sun during the operative condition, the panels are connected without the need of a gimbal mechanism. The choice of placing the SA at the bottom of the S/C is due to the fact that in this configuration the view factor of the radiators, positioned on the rear side of the solar panels, with the deep space is almost unitary and they do not radiate back the heat to the spacecraft. On the other hand the panels can contribute to the thermal regulation of two of the sides of the S/C, through the radiative transfer of part of their thermal energy.

The main electronics are installed in this module, to be close to each other and next to the solar arrays, in order to reduce the length and the mass of the cables. The disposition of the subsystems on the inner side of all the panels allows easy access to the various components, in particular to the batteries, that suffer a progressively discharge in time and require to be mounted right before the actual launch date. In addition, all service dissipative equipment is mounted on the side walls, which provide important mounting surfaces and radiative areas that looks to the deep space.

Concerning the TMTC subsystem, the HGA is mounted on the surface aligned with the $-X_B$ direction, with the Earth always inside its beamwidth, thus achieving constant communication possibility. On the other hand, the LGAs are installed at opposite sides of the spacecraft on booms fixed at the bottom section of the SVM. This positioning ensures omni-directional coverage and avoids signal clogging by the SA.

Regarding the AOCS sensors, the three gyroscopes (only 2 are visible in Figure 18) are disposed along the 3 main axes, while the reaction wheels are disposed in a pyramidal fashion at the corners of the SVM, granting all the required rotations and redundancy.

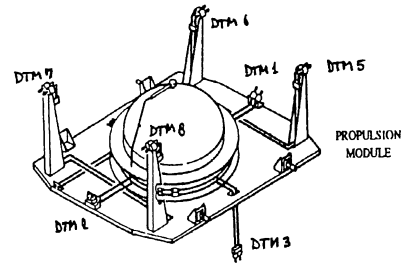


Figure 17: Propulsion module

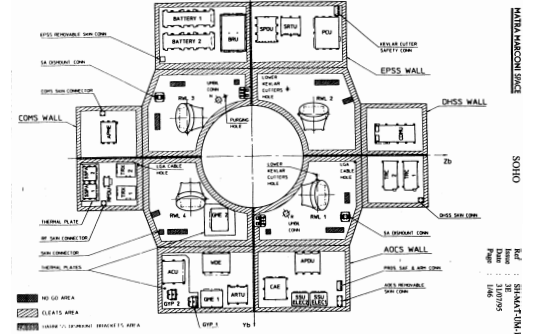


Figure 18: SVM layout

8 On-Board Data Handling Subsystem

8.1 Architecture

For what concerns the on-board data management, proven interfaces have been selected through the use of an ESA OBDH bus for the data handling, and an ESA MACS bus for the AOCS. These two subsystems make use of an identical processor type. In this field, modularity has been achieved thanks to the Remote Terminal Units (RTU), which provide each subsystem (DHSS, AOCS, PLM) with the capability to exchange data with other subsystems through standard interfaces [33].

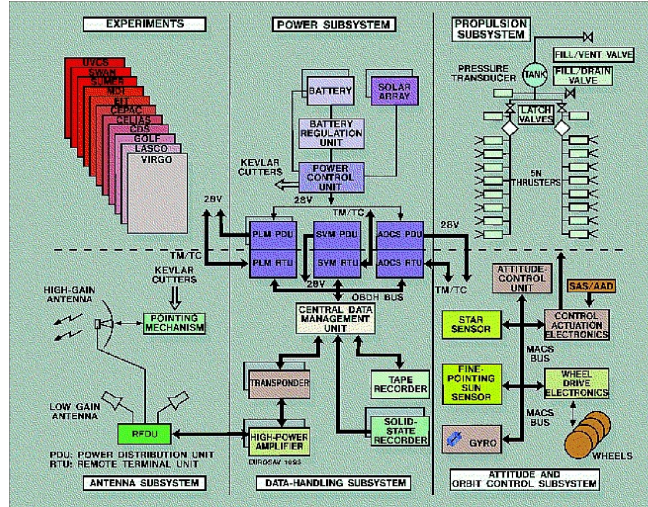


Figure 19: OBDH Scheme

As depicted in Figure 19, the data flow architecture is a centralized one, which is highly reliable and failure-isolated.

The heart of the system is the Central Data Management Unit (CDMU), which includes a 16-bit MAS281 microprocessor. Its tasks are to ensure:

- Telecommands reception, validation and distribution
- Processing of Telecommands whose receiver is the CDMU itself
- Acquisition of data from various predefined OBDH bus users
- Telemetry assembly and sending
- Thermal control of the system
- Antenna pointing
- OBT maintenance and distribution
- Management and surveillance of tape recorders
- Handling of inter-instruments Data Exchange
- Various surveillance functions for the PLM and the SVM
- Execution of the ISA sequence

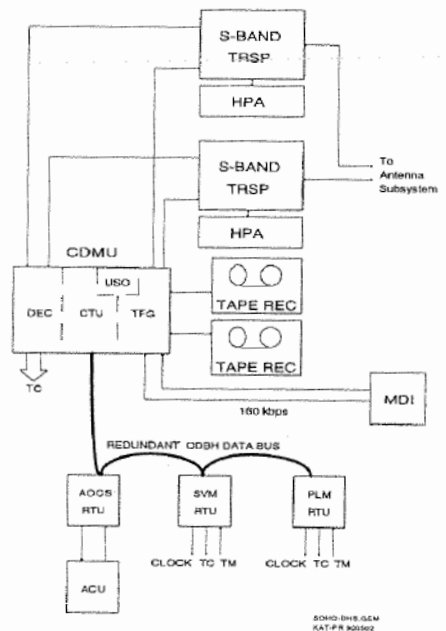


Figure 20: CDMU and OBDH overview

The CDMU interfaces with the following equipment:

- The two S-band transponders, from which it receives telecommands and to which it sends telemetry
- The three RTUs
- The two redundant interfaces to MDI
- The two tape recorders, used for house-keeping and science data

The CDMU addressable memory is *64 kwords*, which may be shared by PROM, RAM and Peripheral Expansion Port (PEP) ROM [34].

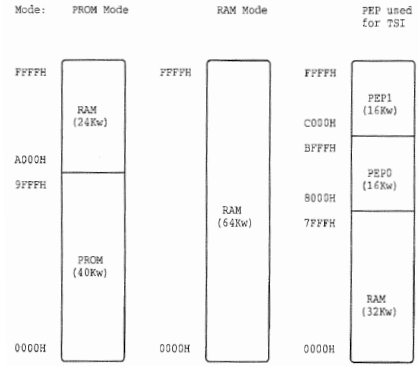


Figure 21: Memory partition

8.2 Sizing

8.2.1 Throughput Sizing

In this section, the sizing of the microprocessors in terms of throughput is performed.

In order to calculate the total KIPS per mode, it is essential to establish the acquisition frequency for each subsystem component.

The acquisition frequency for most components is assumed to be the same as the typical one, except for the SSU, RW, and FPSS in the AOCS¹², TCS and EPS¹³ for which more accurate values have been selected. All the aforementioned values are reported in Figure 28 and Figure 29 in Appendix D. Given the acquisition frequencies, the throughput, quantified in *KIPS*, for each function is computed by similarity, using the typical throughput and the typical acquisition frequency as follows:

$$KIPS_{fun} = \frac{KIPS_{typ} f_{acq}}{f_{typ}} \quad (81)$$

Then, the total throughput is computed:

$$KIPS_{tot} = \sum_{i=1}^{n_{fun}} k_{fun,i} KIPS_{fun,i} \quad (82)$$

where $k_{fun,i}$ is the number of elements for the i -th function and a 400 % margin has been considered.

As previously mentioned in subsection 8.1, there is an identical dedicated microprocessor for the AOCS subsystem. Therefore, the very same computations and considerations are made, analysing the following modes:

- Normal Mode: all AOCS' functions active except thruster control
- Manoeuvre Mode: all AOCS' functions active
- ESR Mode: all AOCS' functions active except star tracker and FPSS

The results for both OBDH and AOCS computed using Equation 81, Equation 82, Figure 28 and Figure 29 (Appendix D) for the three modes of the mission are reported in Figure 22 and Figure 23.

It is important to notice that the P/L contribution is not taken into account since each instrument is provided with its own data handling system.

¹²Regarding the reaction wheels [21], the acquisition frequency is up to 10 Hz, so a value of 2 Hz has been deemed reasonable. For the FPSS [35], a typical value of 2 Hz has been taken in absence of more precise information from the supplier. Regarding the SSU, in absence of the actual datasheet, the one of the second version of the star trackers has been used to estimate an acquisition frequency value, starting from the acquisition time (Lost In Space condition) [36].

¹³For the TCS and the EPS the acquisition frequency used can be found, respectively, in Chapter 5 and 6.

	AOCS	EPS	PS	TCS	TTMTC	PL	OS	TOT [KIPS]
Normal Mode	-	1	0	1	1	0	1	
Throughput [KIPS]	-	0,7	0	0,03	10	0	211	221,73
Margined	-	2,8	0	0,12	40	0	844	886,92

Manoeuvre	-	1	1	1	1	0	1	
Throughput [KIPS]	-	0,7	84	0,03	10	0	211	305,73
Margined	-	2,8	336	0,12	40	0	844	1222,92

ESR	-	1	1	1	1	0	1	
Throughput [KIPS]	-	0,7	84	0,03	10	0	211	305,73
Margined	-	2,8	336	0,12	40	0	844	1222,92

Figure 22: Total throughput needed by each S/S without AOCS

Normal Mode		
TP	338	KIPS
Margined	1352	KIPS
Manoeuvre		
TP	347,6	KIPS
Margined	1390,4	KIPS
ESR		
TP	312,6	KIPS
Margined	1250,4	KIPS

Figure 23: Total throughput needed by AOCS

As it can be noticed from Figure 23, the AOCS throughput is very large with respect to any other subsystem. This is due to the fact that it is the most demanding subsystem in terms of data handling, because of the many functions and the strict requirements in terms of accuracy and pointing, and this is the reason why a dedicated microprocessor has been adopted in the OBDH architecture.

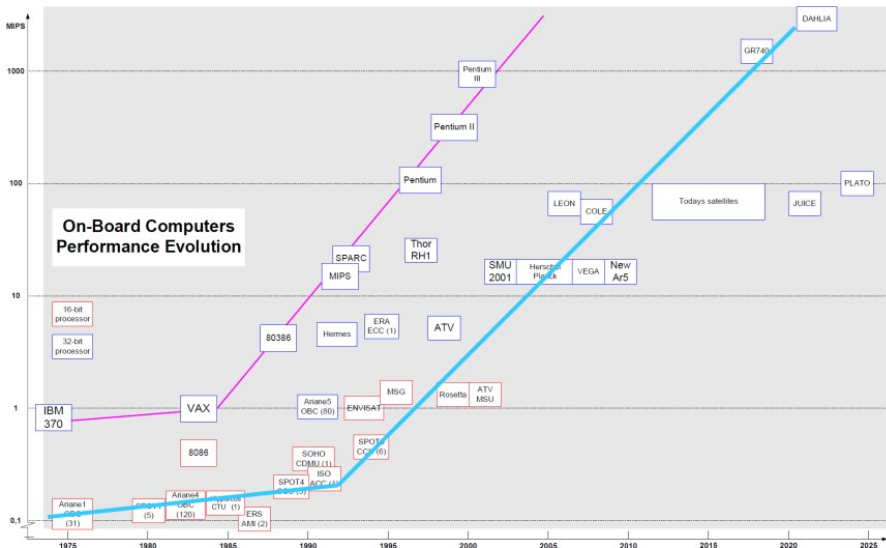


Figure 24: Evolution of processors for space applications

As shown in Figure 24, SOHO's microprocessor's throughput is very low with respect to more recent missions, and it can be noticed that the total throughput is $\approx 0.3 \text{ MIPS}$. Comparing this value with the margined ones computed for each phase, reported in Figure 22 and Figure 23, it comes out being much smaller, and it seems to be closer to the non-margined values. This issue could be due to the

fact that, during the actual OBDH sizing, a much lower margin had been adopted. In fact, margins lower than 400 % are adopted during sizing phases closer in time to the launch.

8.2.2 Memory Sizing

Regarding the code and data, they are stored in the *64 kwords* addressable memory, which can be partitioned in PROM (Programmable ROM), RAM and PEPs depending on the mode.

From Figure 21, it can be seen that the maximum absolute capacities of PROM, RAM and the PEPs are, respectively, *40 kwords* (PROM mode), *64 kwords* (RAM mode) and *16 kwords* for both PEP0 and PEP1. Converting these data in terms of *kB* using $16 \frac{\text{bit}}{\text{word}}$ [37] the memories' sizes read:

$$PROM = \frac{40000 \text{ words} \cdot 16 \frac{\text{bit}}{\text{word}}}{8 \frac{\text{bit}}{\text{B}} \cdot 1000 \frac{\text{B}}{\text{kB}}} = 80 \text{ kB} \quad (83)$$

$$RAM = \frac{64000 \text{ words} \cdot 16 \frac{\text{bit}}{\text{word}}}{8 \frac{\text{bit}}{\text{B}} \cdot 1000 \frac{\text{B}}{\text{kB}}} = 128 \text{ kB} \quad (84)$$

$$PEP = \frac{32000 \text{ words} \cdot 16 \frac{\text{bit}}{\text{word}}}{8 \frac{\text{bit}}{\text{B}} \cdot 1000 \frac{\text{B}}{\text{kB}}} = 64 \text{ kB} \quad (85)$$

For what concerns the AOCS memory, the capacities for PROM and RAM are respectively *32 kwords* and *64 kwords* [23], which lead, using the same formulas as before, to $PROM = 64 \text{ kB}$ and $RAM = 128 \text{ kB}$.

From SOHO's literature [23] a 12 % margin is adopted for the PROM and a 22 % one for the RAM, adding also 8 kB for context memory. On the other hand, the margins on the AOCS memory are much larger and they are equal to 41 % for the PROM and 60 % for the RAM. The results are summarized in the following table:

	OBDH	AOCS
PROM [<i>kB</i>]	80	64
with margin [<i>kB</i>]	89.6	90.24
RAM [<i>kB</i>]	128	128
with margin [<i>kB</i>]	164.16	204.8

Table 26: PROM and RAM size for OBDH and AOCS

It is important to notice that the obtained results are much lower than typical values of the memories used for typical space application. This discrepancy may be generated by different considerations.

Firstly, the evolution of processors and their memory capacity must be taken into account, in order to understand the reason why such a difference occurs between present and past values for PROM and RAM size.

Furthermore, it is important to highlight the environment disturbances under which SOHO is affected. In particular, since electronic devices are prone to suffer from degradation if exposed to radiation, the so called Single Event Effects (SEEs [38]), the solar flux represents a big threat to the whole OBDH subsystem. For this reason, producing a RAM both with a large size and sufficiently reliable in the space environment can be very challenging. This issue is even more problematic for a spacecraft like SOHO, which is constantly pointing the Sun.

Lastly, one key factor for SOHO to have such limited memory is that avionics-related decisions are taken at a very early stage in the spacecraft design process. It typically takes multiple years, sometimes even more than a decade, to progress from initial design to first flight.

References

- [1] R. Short, J. Behuncik. "The Solar and Heliospheric Observatory(SOHO) Mission : An overview of Flight Dynamics Support of the Early Mission Phase". In: () .
- [2] C. E. Roberts. Long term missions at the Sun-Earth libration point L1: ACE, SOHO and WIND.
- [3] C. E. Roberts. "The SOHO Mission L1 halo orbit recovery from the attitude control anomalies of 1998". In: Libration points orbit and application conference (2002).
- [4] URL: <https://www.eoportal.org/satellite-missions/isee-3#spacecraft>.
- [5] A. P. Varia, A. R. Scroggins. "Resurrected DSCOVR Propulsion System - Challenges and Lessons Learned". In: () .
- [6] D.W. Dunham, C.E. Roberts. "Stationkeeping techniques for Liberation-point Satellites". In: The journal of astronautical science (2001).
- [7] J. Long, J. Lorah, E. Malinowski, J. Park, J. Peterson. "Implementation of the Solar Exclusion Zone burn through maneuvers for DSCOVR to preserve fuel for the gyro-less spacecraft in a Sun-Earth L1 Lissajous orbit". In: (2021).
- [8] Northrop Grumman. Datasheet MRE 1.0.
- [9] Ronald Humble. Space Propulsion Analysis and Design. 1995.
- [10] S. Soldini, C. Colombo, S. Walker, M. Landgraf. "Libration-Point Orbit missions disposal at the End-Of-Life through solar radiation pressure". In: IAA-AAS-DyCoSS2 (2014).
- [11] R. M. Bonnet, F. Felici. Overview of the SOHO mission. 1997.
- [12] W. L. Martin, T. Y. Yan, L. V. Lam. CCSDS - SFCG: Efficient modulation methods study at NASA/JPL. 1997.
- [13] CCSDS. Radio frequency and modulation systems. 1989.
- [14] CCSDS. TM synchronization and channel coding. 2023.
- [15] V. Domingo, B. Fleck, A. I. Poland. The SOHO mission: an overview. 1995.
- [16] S.Ougier. R.F Link Budget. 1995.
- [17] Jim Taylor. The Deep Space Network: A Functional Description. 2016.
- [18] URL: <https://eyes.nasa.gov/dsn/dsn.html>.
- [19] RedWire. RAD-HARD Hi-Rel datasheet.
- [20] URL: https://indico.esa.int/event/182/contributions/1506/attachments/1456/1682/1710_-_Boldrini.pdf.
- [21] Bradford Engineering. Bradford Reaction Wheel Unit.
- [22] URL: <https://solar.bnsc.rl.ac.uk/scientificops/bluebook/chapter08.pdf>.
- [23] URL: <https://www.esa.int/esapub/bulletin/bullet84/vdbus84.htm>.
- [24] URL: <https://soho.nascom.nasa.gov/soc/esr/>.
- [25] R.D. Headrick, J.N. Rowe. SOHO Flight Dynamics Simulations using MATLAB.
- [26] J. L. Garcia. SOHO SVM thermal control. 1994.
- [27] P.Poinas, J.Candè. SOHO spacecraft thermal control aspect.
- [28] P. Rumler, H. Schweitzer. SOHO power system performance during 6 years in orbit. 2002.
- [29] P. Rumler, H. Schweitzer, H. Evans. SOHO Solar Array. 1998.
- [30] R. H. A. van Hassel. The ARA Mark 3 Solar Array and Development. 1995.
- [31] EASE. Nickel-Cadmium battery.
- [32] URL: <http://swan.projet.latmos.ipsl.fr/papers/BertauxEtAl1995.pdf>.
- [33] M. Bouffard, J.P. Gardelle, M. Le Moine, P. Temporelli. "SOHO : a modular spacecraft concept to allow flexible payload integration and efficient development". In: (1995).

- [34] Saab Ericsson Space. CDMU Hardware Overview. 1996.
- [35] Redwire. Fine Pointing Sun Sensor.
- [36] Leonardo Airborne & Space Systems. AUTONOMOUS STAR TRACKERS. 2017.
- [37] Dynex Semiconductor. MAS281 MIL-STD-1750A Microprocessor. 2000.
- [38] NASA. Single Event Effects. URL: <https://radhome.gsfc.nasa.gov/radhome/see.htm>.
- [39] ESA. SOHO Fact Sheet. 2003.
- [40] NASA, ESA. Solar and Heliospheric Observatory. URL: <https://soho.nascom.nasa.gov/>.
- [41] V. Domingo, B. Fleck, A. I. Poland. SOHO - Science Operations Plan. 1995.
- [42] O. C. St. Cyr, L. Sánchez-Duarte. SOHO Ground Segment, Science operation and Data Products.
- [43] W. Worrall, D. Muñonen, R. Menrad. The SOHO Ground Segment and Operations. URL: <https://www.esa.int/esapub/bulletin/bullet84/worral84.htm>.
- [44] URL: <https://nssdc.gsfc.nasa.gov/nmc/spacecraft/displayTelemetry.action?id=1995-065A>.
- [45] URL: <https://www.copernical.com/projects-public/item/18243-soho-solar-and-heliospheric-observatory>.

Appendix

Appendix A - Chapter 4

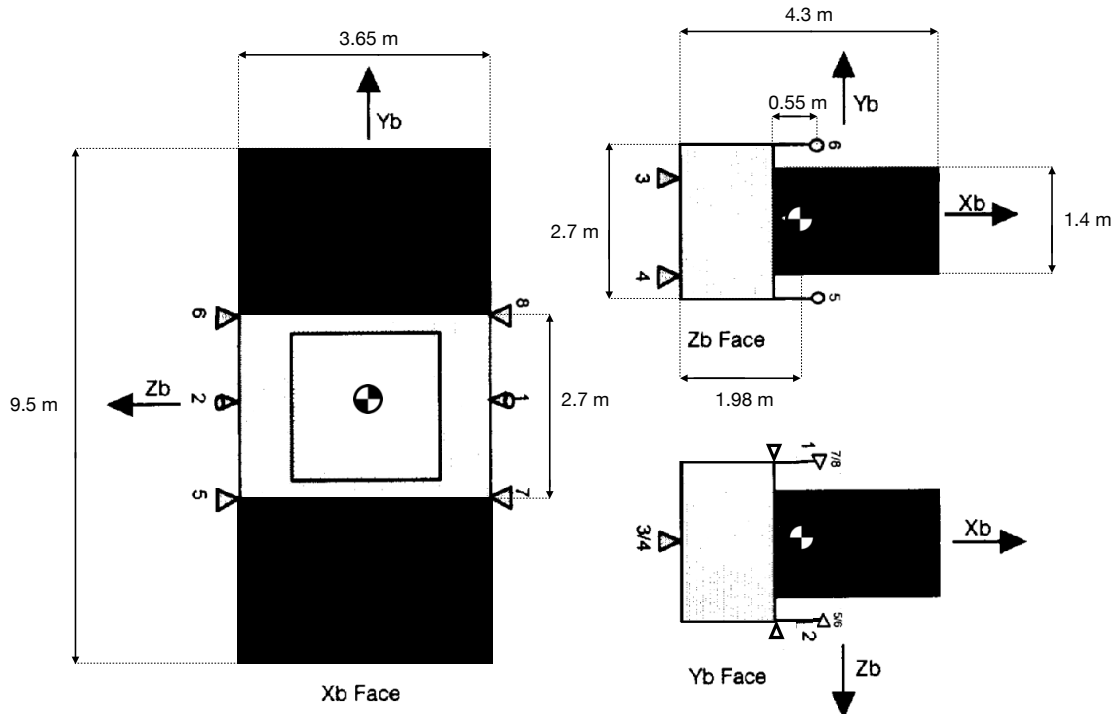


Figure 25: S/C dimensions and thrusters configuration

Thruster Pair	Thruster Location	Δv Direction (body frame)	Primary Attitude Control	Thrust X_B -cosine	Thrust Z_B -cosine
1 and 2	Sunward	$-X_B$	Pitch	-0.866	+0.5 (1) -0.5 (2)
3 and 4	Earthward	$+X_B$	Yaw	+1	0
5 and 6	Top	$-Z_B$	Roll	0	-1
7 and 8	Bottom	$+Z_B$	Roll	0	+1

Table 27: Thrusters position and direction

Which leads to the following configuration matrix:

$$\mathbf{R} = \begin{bmatrix} 0 & 0 & 0 & 0 & -1.3500 & 1.3500 & 1.3500 & -1.3500 \\ -1.7722 & 1.7722 & 0 & 0 & -0.1665 & -0.1665 & 0.1665 & 0.1665 \\ 0 & 0 & 0.7000 & -0.7000 & 0 & 0 & 0 & 0 \end{bmatrix} m$$

such that $\mathbf{M} = \mathbf{R} \times \mathbf{T}$.

Appendix B - Chapter 5

The heat fluxes per unit area are determined considering a direct dependence on the distance from the different emitters:

$$\dot{q}_{Sun-S/C} = \dot{q}_0 \left(\frac{R_{Sun-Earth}}{R_{Sun-S/C}} \right)^2 \quad (86)$$

$$\dot{q}_{albedo} = \dot{q}_{Sun-S/C} a \cos\theta \left(\frac{R_{Earth}}{R_{Earth-S/C}} \right)^2 \quad (87)$$

$$\dot{q}_{IR} = \sigma_0 \epsilon_{Earth} T_{Earth}^4 \left(\frac{R_{Earth}}{R_{Earth-S/C}} \right)^2 \quad (88)$$

Appendix C - Chapter 7

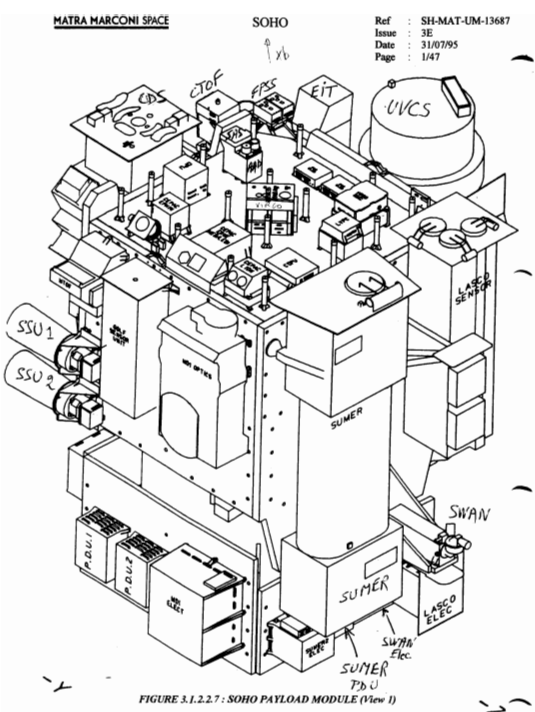


Figure 26: Payload Module without sun shield



Figure 27: Tilted configuration

Appendix D - Chapter 8

PS					
Components	#	Typical KIPS	Typical Frequency [Hz]	Acquisition Frequency [Hz]	KIPS
Tank	1	-	-	-	-
Tank Control Valve	14	3,00	0,10	0,10	3
Tank Pressure Sensor	14	3,00	0,10	0,10	3

EPS					
Components	#	Typical KIPS	Typical Frequency [Hz]	Acquisition Frequency [Hz]	KIPS
Solar Panels	2	-	-	-	-
Batteries	2	-	-	-	-
Cable & Harness	1	-	-	-	-
Power voltage control	1	5,00	1,00	0,07	0,35
Power current control	1	5,00	1,00	0,07	0,35

TCS					
Components	#	Typical KIPS	Typical Frequency [Hz]	Acquisition Frequency [Hz]	KIPS
Thermal Control	1	3,00	0,10	0,001	0,03

TTMTC					
Components	#	Typical KIPS	Typical Frequency [Hz]	Acquisition Frequency [Hz]	KIPS
S-Band HGA	1	-	-	-	-
S-Band LGA	2	-	-	-	-
Transponder (Uplink)	1	7,00	10,00	10,00	7
Transponder (Downlink)	1	3,00	10,00	10,00	3

System					
Components	#	Typical KIPS	Typical Frequency [Hz]	Acquisition Frequency [Hz]	KIPS
I/O Device Handlers	1	50,00	5,00	5,00	50
Test and Diagnostic	1	0,50	0,10	0,10	0,5
Math Utilities	1	0,50	0,10	0,10	0,5
Executive	1	60,00	10,00	10,00	60
Run Time Kernel	1	60,00	10,00	10,00	60
Complex Autonomy	1	20,00	10,00	10,00	20
Fault Detection (monitors)	1	15,00	5,00	5,00	15
Fault Correction	1	5,00	5,00	5,00	5

Figure 28: Acquisition frequency and KIPS of all subsystems without AOCS

AOCS					
Components	#	Typical KIPS	Typical Frequency [Hz]	Acquisition Frequency [Hz]	KIPS
RW	3	5,00	2,00	2,00	5
Thruster Control	8	1,20	2,00	2,00	1,2
Star Tracker	1	2,00	0,01	0,17	34
Gyros	3	9,00	10,00	10,00	9
FPSS	1	1,00	2,00	2,00	1
Kinematic Integration	1	15,00	10,00	10,00	15
Error Determination	1	12,00	10,00	10,00	12
Attitude Determination	1	150,00	10,00	10,00	150
Attitude Control	1	60,00	10,00	10,00	60
Complex Ephemeris	1	4,00	0,50	0,50	4
Orbit Propagation	1	20,00	1,00	1,00	20

Figure 29: Acquisition frequency and KIPS of AOCS